Journal of Photochemistry & Photobiology, A: Chemistry 478 (2026) 117194

Contents lists available at ScienceDirect

Journal of Photochemistry & Photobiology, A: Chemistry

journal homepage: www.elsevier.com/locate/jphotochem

Charge-compensated $LiCa_4O(BO_3)_3$:Tb^{3+} phosphors: K^+/Na^+-assisted lattice engineering for thermally robust green emission and luminescent thermometry

Abeer S. Altowyan [a,*], M.B. Coban [b,c], U.H. Kaynar [d], R. Tulek [b], A. Teke [b], Y. Ozcan [e], Jabir Hakami [f], H. Aydin [g,h], N. Can [f,*]

[a] Department of Physics, College of Science, Princess Nourah Bint Abdulrahman University, P.O. Box 84428, Riyadh 11671, Saudi Arabia
[b] Faculty of Arts and Sciences, Department of Physics, Balikesir University, Balikesir, Turkiye
[c] Science and Technology Application and Research Center, Balikesir University, Balikesir, Turkiye
[d] Faculty of Engineering and Architecture, Department of Fundamental Sciences, Bakircay University, Menemen, Izmir, Turkiye
[e] Department of Biomedical Engineering, Faculty of Technology, Pamukkale University, 20070 Denizli, Turkiye
[f] College of Science, Department of Physical Sciences, Physics Division, Jazan University, P.O. Box 114, 45142 Jazan, Saudi Arabia
[g] Central Research Laboratories, Izmir Katip Celebi University, Izmir, Turkiye
[h] Graphene Application & Research Center, Izmir Katip Celebi University, Izmir, Turkiye

ARTICLE INFO

Keywords:
$LiCa_4O(BO_3)_3$ phosphors
Tb^{3+}-activated borates
Alkali-ion charge compensation
Green photoluminescence
Luminescent thermometry

ABSTRACT

Tb^{3+}-activated $LiCa_4O(BO_3)_3$ (LiCBO) borates are promising phosphors for high-power near-UV LEDs and optical thermometry, but charge imbalance and lattice defects limit their thermal stability and efficiency. This work reports a comprehensive structural–optical study of LiCBO:Tb^{3+} phosphors with K^+/Na^+ charge-compensating co-dopants synthesized by combustion reaction. X-ray diffraction and Rietveld refinement show that all compositions remain single-phase LiCBO, with Tb^{3+} preferentially substituting Ca^{2+} sites while K^+/Na^+ ions act as charge compensators, inducing only marginal, monotonic changes in lattice parameters. Multi-model XRD line-broadening analysis reveals that alkali co-doping increases crystallite size from ~60 to ~90 nm and reduces microstrain and dislocation density, indicating defect suppression through charge-compensated lattice engineering. FTIR/Raman spectroscopy confirms preservation of the mixed BO_3/BO_4 framework, with subtle band shifts and increased $I(BO_4)/I(BO_3)$ ratios evidencing local network reorganization rather than phase segregation. Under 377 nm excitation, LiCBO:Tb^{3+} exhibits intense green $^5D_4 \rightarrow {}^7F_5$ emission at 542 nm with an optimum Tb^{3+} content of $x = 0.05$, above which concentration quenching proceeds via multipolar Tb^{3+}–Tb^{3+} interactions ($R_c \approx 10.6$ Å). K^+/Na^+ co-doping boosts the green emission by up to ~2–2.25× at $y = 0.01$, mainly by suppressing non-radiative defect channels and tuning local symmetry, as supported by biexponential lifetime shortening and increased Judd–Ofelt Ω_2 parameters. Temperature-dependent PL (300–550 K) demonstrates robust thermal stability, retaining ~40–45% of the initial 542 nm intensity at 423–450 K with a single activation energy $E_a \approx 0.33$ eV. Finally, a fluorescence intensity ratio thermometer based on the 680/542 nm Tb^{3+} emissions delivers a maximum relative sensitivity of ~1.3% K^{-1} near 500 K, demonstrating competitive performance among single-center Tb^{3+}-activated phosphors for high-temperature operation. Overall, K^+/Na^+-assisted charge-compensated lattice engineering is shown to simultaneously enhance green emission efficiency, thermal robustness, and luminescent thermometry performance in LiCBO:Tb^{3+} phosphors.

1. Introduction

Rare-earth-ion-doped inorganic phosphors constitute a fundamental class of luminescent materials for solid-state lighting, display technologies, optical sensing, and photonic applications due to their sharp emission lines, high color purity, and excellent chemical stability [1,2]. These characteristics originate from the shielded nature of the 4f electronic orbitals, which weakly interact with the host lattice and result

* Corresponding authors.
E-mail addresses: asaltowyan@pnu.edu.sa (A.S. Altowyan), ncan@jazanu.edu.sa (N. Can).

https://doi.org/10.1016/j.jphotochem.2026.117194
Received 25 January 2026; Received in revised form 3 March 2026; Accepted 10 March 2026
Available online 14 March 2026

in parity-forbidden but spectrally narrow 4f–4f transitions largely insensitive to external perturbations [3].

Among various rare-earth activators, terbium ions (Tb^{3+}) are particularly attractive because of their intense green emission arising from the $^5D_4 \rightarrow {}^7F_J$ transitions, which are well suited for lighting and display applications requiring high chromatic purity [4,5]. The luminescent efficiency of Tb^{3+}-activated phosphors is strongly governed by the local crystal field symmetry and site occupation of the activator ions, which control the balance between radiative transitions and non-radiative relaxation pathways [6,7].

With the increasing demand for high-power light-emitting devices, the thermal stability of phosphor materials has become a critical performance parameter. Elevated operating temperatures can induce thermal quenching via enhanced multiphonon relaxation and thermally activated processes (e.g., crossover or ionization), leading to significant emission loss [8,9]. Consequently, the development of host lattices capable of maintaining efficient Tb^{3+} emission over a wide temperature range remains a central challenge in contemporary phosphor research.

Borate-based host lattices have been extensively investigated for rare-earth-activated phosphors due to their low phonon energies, rigid anionic frameworks, and high chemical and thermal stability [10–15]. The presence of covalently bonded BO_3 units results in reduced multiphonon relaxation probabilities, thereby favouring radiative recombination of excited rare-earth ions. In addition, borate compounds often exhibit wide optical transparency windows and good structural tolerance toward aliovalent substitution, making them suitable platforms for luminescent applications under demanding operating conditions [16].

Lithium–calcium borate systems are particularly attractive because of their structural flexibility and ability to accommodate multiple cation species within the lattice. The coexistence of monovalent and divalent cations enables effective charge compensation mechanisms when trivalent rare-earth ions are introduced, thereby minimizing lattice distortion and defect-assisted non-radiative losses [17–20]. Furthermore, the mixed-cation framework can influence the local coordination environment of activator ions, which is crucial for tailoring crystal field symmetry and emission characteristics.

Among various borate hosts, LiCBO offers a stable crystalline framework with multiple cationic sites that are potentially accessible to rare-earth dopants. Recent studies have demonstrated that alkali-metal co-doping in Eu^{3+}-activated LiCBO can effectively modulate local site symmetry, Judd–Ofelt parameters, and thermal stability through charge-compensated lattice modification [21]. However, systematic investigations on Tb^{3+}-activated LiCBO phosphors remain scarce, particularly with respect to activator-specific luminescence mechanisms, charge-compensation effects, and high-temperature photoluminescence behavior. This gap motivates a detailed exploration of Tb^{3+} incorporation and alkali-metal-assisted lattice modification in this host system.

The incorporation of Tb^{3+} ions into oxide-based host lattices is often accompanied by charge imbalance and local lattice distortion, particularly when Tb^{3+} substitutes divalent cation sites. In lithium–calcium borate hosts, the replacement of Ca^{2+} by Tb^{3+} introduces excess positive charge, which can promote defect formation and enhance non-radiative relaxation if not properly compensated. Such effects are especially detrimental for Tb^{3+}-activated phosphors, where emission efficiency and thermal stability are highly sensitive to the local coordination environment. Alkali-metal co-doping represents an effective strategy to address these limitations by providing charge compensation and structural modulation within the host lattice [22–24]. The introduction of monovalent Li^+ or Na^+ ions can balance the charge mismatch induced by Tb^{3+} substitution while simultaneously influencing lattice rigidity and local crystal field symmetry. This dual role enables suppression of defect-assisted non-radiative pathways and optimization of Tb^{3+} site symmetry, which is critical for enhancing the $^5D_4 \rightarrow {}^7F_J$ emission efficiency [25].

Furthermore, Li^+ and Na^+ ions differ in ionic radius and polarizability, leading to distinct impacts on lattice distortion, phonon environment, and Tb^{3+}–Tb^{3+} interaction distances [23,26,27]. Such differences are expected to affect concentration quenching behavior, Judd–Ofelt intensity parameters, and temperature-dependent luminescence characteristics. Consequently, a comparative investigation of Li^+- and Na^+-assisted co-doping provides valuable insight into the structure–property relationships governing Tb^{3+} luminescence in lithium–calcium borate hosts.

Recently, borate-based phosphors have attracted renewed attention owing to their structural rigidity, relatively low phonon energies, and chemical stability, which are advantageous for both solid-state lighting (SSL) and thermometric applications. Several studies have reported enhanced luminescence efficiency, improved thermal robustness, and tunable chromatic properties in rare-earth-doped borate hosts such as $Ca_3B_2O_6:Eu^{3+}$[28], $Y_2CaB_{10}O_{19}:Dy^{3+}$ [29], $Sr_3B_{14}O_{24}:RE^{3+}$ [30], $Sr_3Y_2B_4O_{12}$:Ce/Tb/Sm [31], and alkali rare-earth borates $A_3Ln(BO_3)_2$ (A = Na, K) [32]. In particular, recent investigations have emphasized the role of compositional engineering and alkali-metal-assisted charge compensation in stabilizing emission centers and improving high-temperature performance. Despite these advances, systematic studies addressing charge-compensated Tb^{3+} activation in $LiCa_4O(BO_3)_3$ and its impact on high-temperature FIR thermometry and chromatic stability remain limited.

In this work, Tb^{3+}-activated LiCBO phosphors were systematically synthesized with Li^+ and Na^+ as charge-compensating co-dopants to elucidate the interplay between lattice modification, local site symmetry, and luminescence behavior. Phase purity and structural evolution were examined using X-ray diffraction combined with Rietveld refinement, while microstructural features and elemental distributions were analyzed by SEM–EDS. Vibrational characteristics and local bonding environments were investigated through FTIR and Raman spectroscopy. The photoluminescence properties were evaluated under both room-temperature and elevated-temperature conditions to assess emission efficiency and thermal stability. Furthermore, Judd–Ofelt analysis was employed to quantify the local symmetry and radiative transition probabilities of Tb^{3+} ions, and chromaticity coordinates were derived to correlate structural modulation with color output.

To the best of our knowledge, a comprehensive study addressing Tb^{3+}-activated LiCBO phosphors with a comparative Li^+/Na^+ co-doping strategy remains unexplored. Unlike prior investigations primarily focused on Eu^{3+}-based systems or single-alkali modification, the present work highlights activator-specific luminescence mechanisms of Tb^{3+} and reveals how distinct alkali ions differentially regulate charge compensation, crystal field symmetry, and thermal quenching behavior. In a closely related structural family, temperature-sensitive photoluminescence behavior and defect-related broadband emission have been reported for $LaCa_4O(BO_3)_3:Tb^{3+}$ phosphors, highlighting the intrinsic role of lattice defects and local structural disorder in governing thermal emission stability in alkaline-earth borate hosts [33]. The insights gained from this study provide a coherent structure–property–performance relationship, offering practical guidelines for the rational design of thermally robust green-emitting borate phosphors for solid-state lighting and related photonic applications, with particular emphasis on preserving efficient Tb^{3+} green emission under high-power near-UV LED pumping conditions, where photoluminescence stability up to ~150–200 °C is a critical performance requirement [34].

2. Experiments

2.1. Materials and synthesis

The crystal structure and phase purity of the prepared phosphor samples were examined by X-ray diffraction (XRD) using a Malvern PANalytical Empyrean diffractometer operated at 45 kV and 40 mA with Cu Kα radiation (λ = 1.5406 Å). Fourier transform infrared (FTIR) spectra were acquired in the 400–4000 cm^{-1} region with a Thermo

Scientific Nicolet iS50 spectrometer in attenuated total reflectance (ATR) configuration. Raman spectroscopy was carried out on a Renishaw inVia Raman microscope equipped with a 532 nm excitation source to investigate local vibrational modes and bonding features of the host lattice. Surface morphology and elemental distribution of the phosphors were characterized using a Zeiss scanning electron microscope (SEM) coupled with an energy-dispersive X-ray spectroscopy (EDS) system. Photoluminescence excitation and emission spectra at room temperature were measured on an Edinburgh Instruments FS5 spectrofluorometer equipped with a xenon lamp and double monochromators. All photoluminescence measurements were performed under identical experimental conditions for each composition to enable reliable comparison.

2.2. Synthesis of $LiCa_4O(BO_3)_3:Tb^{3+}$ phosphors

LiCBO phosphors were synthesized by a sol–gel combustion route using urea as the organic fuel. All reagents were of analytical grade and used as received without further purification: lithium nitrate ($LiNO_3$, Sigma, ≥99.99%), calcium nitrate ($Ca(NO_3)_2{\cdot}xH_2O$, Sigma-Aldrich, ≥99.9%), boric acid (H_3BO_3, Merck), urea ($CO(NH_2)_2$), terbium nitrate ($Tb(NO_3)_3{\cdot}xH_2O$), sodium nitrate ($NaNO_3$, Merck, 99.9%), and potassium nitrate (KNO_3, Merck, 99.9%). Tb^{3+} ions were employed as activators with concentrations of 0.5, 1, 2, 3, 5, and 7 wt%, while Na^+ or K^+ ions were introduced separately as charge-compensating co-dopants at matching molar ratios.

In a typical synthesis, stoichiometric amounts of $LiNO_3$ and $Ca(NO_3)_2$ were dissolved in 20 mL of deionized water in a quartz beaker. Subsequently, H_3BO_3 and urea were added under continuous stirring. For doped samples, appropriate amounts of $Tb(NO_3)_3$ together with $NaNO_3$ or KNO_3 were introduced into the solution. The resulting mixture was magnetically stirred at 80 °C for 1 h under a covered beaker to ensure complete dissolution and homogenization, followed by additional stirring at the same temperature with the cover removed to allow gradual evaporation of excess water. This process yielded a dark, viscous gel.

The obtained gel was subjected to microwave-assisted ignition in a domestic microwave oven operating at 800 W for approximately 3–5 min until self-ignition occurred. Within a short time, a vigorous self-sustained combustion accompanied by copious gas evolution occurred, producing a voluminous, foamy, ash-like precursor powder.

The as-combusted products were subsequently calcined in air at 800 °C for 2 h with a heating rate of 5 °C min^{-1} and natural furnace cooling to room temperature to remove residual organics and improve crystallinity. The simplified overall combustion reaction can be expressed as:

$$2\ LiNO_3 + 8\ ca(NO_3)_2 + 6H_3BO_3 + 3\ CO(NH_2)_2 \rightarrow 2\ LiCa_4O(BO_3)_3 + \text{gaseous products } (NO_x,\ CO_2,\ H_2O,\ NH_3,\ \ldots)$$

To ensure experimental reproducibility, the complete synthesis procedure was independently repeated at least three times for representative compositions (undoped, $0.05Tb^{3+}$, $0.05Tb^{3+}$–$0.01Na^+$ and $0.05Tb^{3+}$–$0.01\ K^+$) under identical precursor purities, weight ratios, solution volumes, microwave power, and calcination profiles. XRD patterns of independently prepared batches were indistinguishable within instrumental resolution, confirming phase purity and structural consistency. The integrated photoluminescence intensity of the 542 nm emission varied within ±5–7% between batches measured under identical instrumental conditions, while refined lattice parameters differed by less than 0.2% within experimental uncertainty, demonstrating good reproducibility of the synthesis protocol.

After calcination, the resulting white, nanocrystalline LiCBO powders were cooled to room temperature and stored in a desiccator prior to further characterization.

3. Results and discussions

3.1. Structural evolution and charge-compensated lattice modulation in Tb^{3+}-activated $LiCa_4O(BO_3)_3$

The phase purity and structural stability of Tb^{3+}-activated LiCBO phosphors, with and without alkali-metal co-doping, were first examined by X-ray diffraction. As shown in Fig. 1a, all diffraction patterns can be consistently indexed to the standard LiCBO phase, confirming that Tb^{3+} incorporation and subsequent Li^+/Na^+ co-doping do not alter the parent crystal structure. [19,26]. No secondary phases were detected within the instrumental resolution, indicating the successful incorporation of Tb^{3+} and alkali ions into the host lattice without detectable phase segregation [33,35].

To evaluate the feasibility of Tb^{3+} substitution within the lattice, an ionic radius mismatch analysis was carried out using Shannon's effective ionic radii, as summarized in Table 1. For Ca^{2+} in VIII-fold coordination and Tb^{3+} in the same environment, the Shannon radii are approximately 1.12 Å and 1.04 Å, respectively, giving $\Delta r \approx 7.1\%$, whereas the mismatch between Tb^{3+} and Li^+ ($r \approx 0.92$ Å, CN = 4) exceeds 10–15% depending on the assumed coordination, clearly differentiating the two possible substitution sites [31]. The calculated radius difference (Δr) between Tb^{3+} and Ca^{2+} remains well below the commonly accepted threshold of 30%, indicating that Tb^{3+} can preferentially occupy Ca^{2+} sites with minimal lattice strain [36,37]. This assignment is further supported by the coordination environment of Ca^{2+} in LiCBO, which offers a chemically reasonable match to the preferred coordination of Tb^{3+} in oxide hosts. This substitution scenario ($Tb^{3+} \rightarrow Ca^{2+}$) is consistent with previous analyses on rare-earth-doped borate hosts, where RE^{3+} ions favor alkaline-earth or rare-earth cation sites while alkali ions act as charge compensators [35]. In contrast, the substantially larger mismatch associated with Li^+ sites suggests that direct Tb^{3+} substitution at these positions is energetically unfavorable, in qualitative agreement with studies on layered and perovskite-type oxides where oversize dopants at Li^+ sites induce pronounced lattice distortion and degraded functional properties [38,39]. These considerations point to a dominant substitution mechanism in which Tb^{3+} ions replace Ca^{2+} ions, while monovalent alkali ions are incorporated as charge compensators to maintain local charge neutrality.

A schematic representation of the LiCBO crystal structure is presented in Fig. 1b to illustrate the charge-compensated lattice configuration. The model highlights the occupation of Ca^{2+} sites by Tb^{3+} ions and the spatial role of Li^+/Na^+ ions in balancing the excess positive charge introduced by aliovalent substitution. The rigid BO_3 units form a stable borate backbone, which constrains excessive lattice relaxation and limits the formation of defect centers, thereby preserving long-range structural order, in agreement with observations that borate frameworks tend to remain intact under aliovalent doping, while alkali co-doping primarily tunes local symmetry and defect chemistry [26].

Rietveld refinement was performed to further quantify the structural integrity and subtle lattice modulation induced by Tb^{3+} doping and alkali-metal co-doping, with a representative refinement profile shown in Fig. 1c. The refined lattice parameters of the undoped LiCBO phase were determined as $a \approx 6.08$ Å, $b \approx 13.28$ Å, and $c \approx 6.18$ Å. Upon Tb^{3+} incorporation (0.05 fraction), only marginal changes were observed, with lattice constants of $a \approx 6.08$ Å, $b \approx 13.28$ Å, and $c \approx 6.18$ Å, indicating that the host lattice accommodates the aliovalent substitution without significant structural disruption. Such small, monotonic variations in lattice parameters and unit-cell volume upon rare-earth/alkali co-doping are typical of charge-compensated borate and phosphite phosphors [23,33].

The unit cell volume exhibits a similarly limited variation, increasing slightly from approximately 499.38 $Å^3$ for the undoped sample to about 499.73 $Å^3$ at higher Tb^{3+} concentrations, consistent with minor local lattice expansion arising from ionic radius mismatch. The quality of the refinements is confirmed by low reliability factors, with R_p values in the

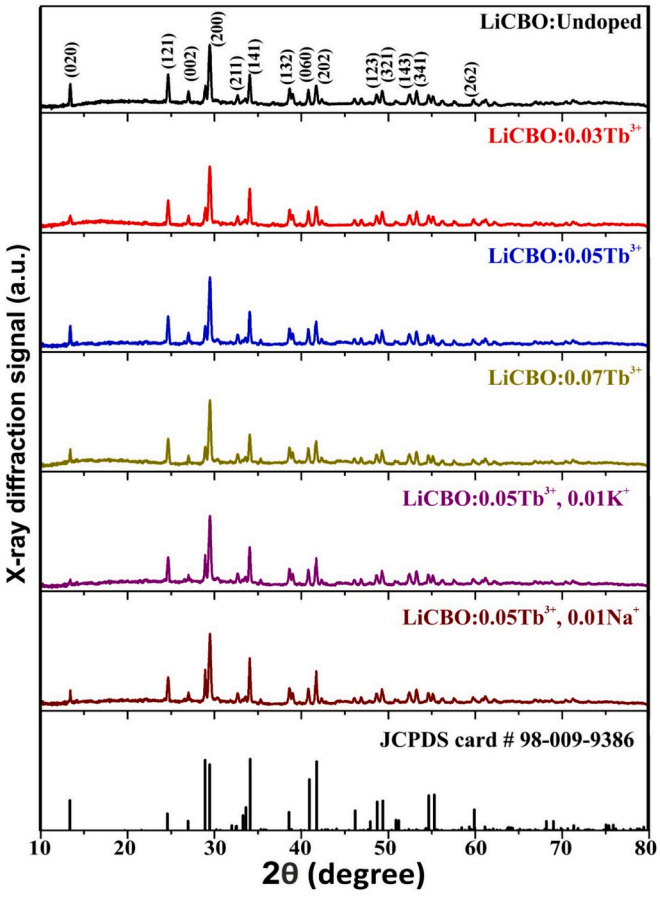

(a)

Fig. 1. (a) X-ray diffraction patterns of undoped and Tb^{3+}-doped LiCBO phosphors with and without alkali-metal co-doping, compared with the standard LiCBO phase (JCPDS card No. 98–009-9386). (b) Schematic representation of the LiCBO crystal structure illustrating the substitution of Tb^{3+} ions at Ca^{2+} sites and the role of Li^{+}/Na^{+} ions in charge compensation within the rigid BO_3 framework. (c) Rietveld refinement profile of a representative Tb^{3+}-doped LiCBO sample, showing the observed, calculated, and difference patterns.

range of 0.109–0.114, R_{wp} values between 0.167 and 0.173, and $R_{exp} \approx$ 0.040, demonstrating excellent agreement between the observed and calculated diffraction patterns. These R_p and R_{wp} values, which remain well below ~0.2, are characteristic of reliable structural models in powder Rietveld refinement and indicate that no major structural misfit or hidden secondary phases are present. These refinement indices are comparable to or better than those reported for other Tb^{3+}-activated and alkali-co-doped oxide hosts [40,41]. The refined structural parameters for all compositions are summarized in Table 2.

Overall, the combined XRD analysis, ionic radius evaluation, structural schematic, and Rietveld refinement results demonstrate that alkali-metal co-doping effectively stabilizes the Tb^{3+}-substituted LiCBO lattice by compensating charge imbalance and moderating local lattice distortion. This charge-compensated structural robustness is consistent with the luminescence enhancements observed in alkali-co-doped Tb^{3+} phosphors, where improved crystallinity and reduced defect densities suppress non-radiative losses [42,43]. Such a stabilized lattice provides a reliable foundation for suppressing defect-assisted non-radiative pathways and is essential for achieving efficient and thermally stable Tb^{3+}-activated photoluminescence, as discussed in the following sections.

3.2. Crystalline size and lattice strain analysis

The crystallite size and microstructural strain of Tb^{3+}-doped and alkali co-doped LiCBO phosphors were systematically evaluated using multiple line-broadening approaches (Debye–Scherrer, Monshi–Scherrer, Williamson–Hall, Halder–Wagner and size–strain plot), ensuring a reliable separation of size- and strain-induced contributions similar to established XRD peak-profile studies on oxides and phosphors [44,45]. Fig. 2a presents the Monshi–Scherrer plots, where a gradual increase in crystallite size is observed with increasing Tb^{3+} concentration, indicating enhanced crystallinity upon activator incorporation. This trend is consistent with reports where rare-earth or flux co-doping promotes grain growth and reduces defect density [23,46]. Notably, alkali co-doping further promotes grain growth, with the $0.05Tb^{3+}$–0.01 K^{+} sample exhibiting the largest average crystallite size, consistent with reduced lattice disorder.

The Williamson–Hall analysis (Fig. 2b) reveals a non-negligible contribution of microstrain, particularly for intermediate Tb^{3+} concentrations. While Tb^{3+} substitution introduces local lattice distortion due to charge and size mismatch with Ca^{2+}, the incorporation of alkali ions partially compensates for this effect, leading to a redistribution of strain within the lattice. This type of dopant-induced distortion and its mitigation by co-doping are commonly observed in oxide and borate hosts [47,48]. This behavior is reflected by the reduced slope values for the co-doped samples, especially in the Na^{+}-assisted composition, suggesting more homogeneous strain accommodation.

Further insight is obtained from the Halder–Wagner method (Fig. 2c), which emphasizes strain-weighted broadening and confirms the trend of increasing crystallite size with alkali co-doping. In line with comparative HW–W–H studies, HW typically yields slightly lower strain

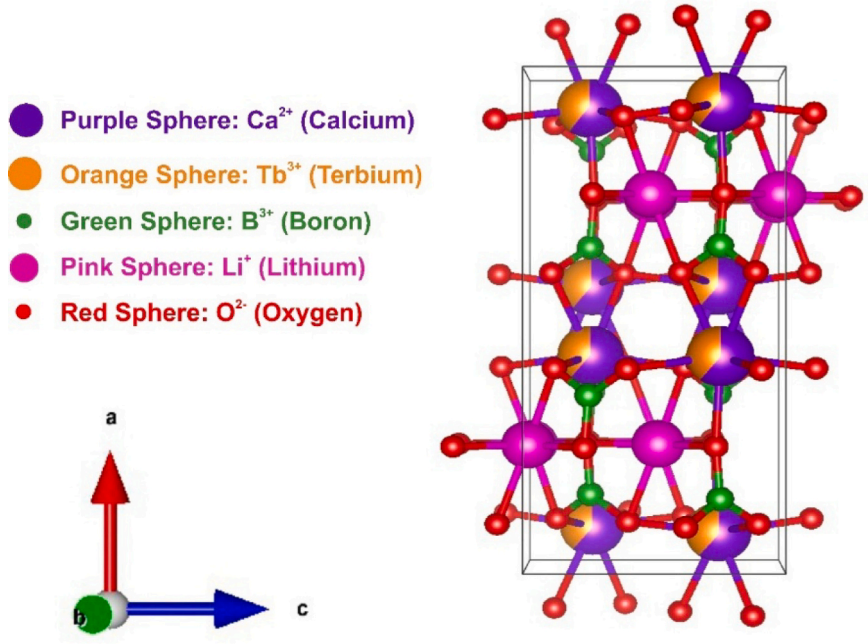

(b)

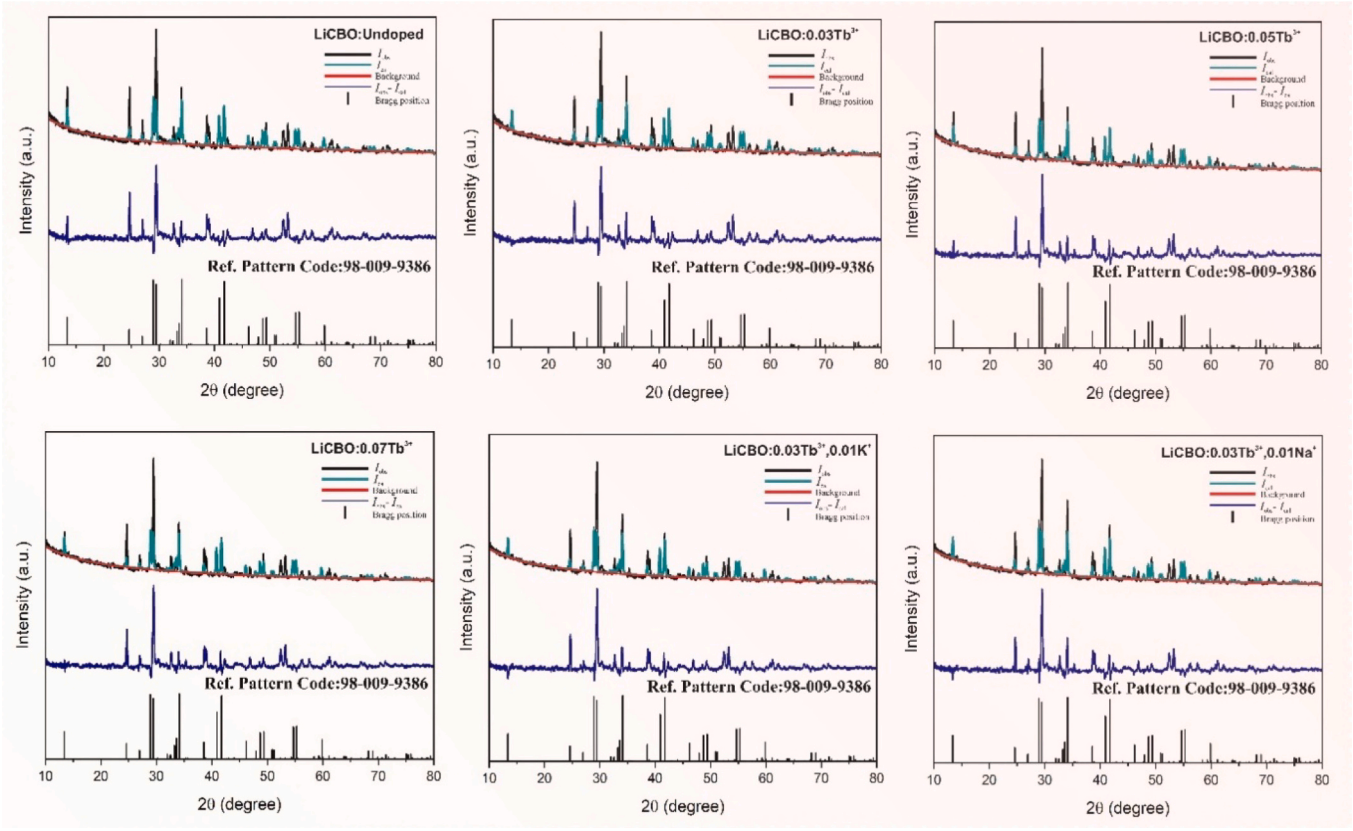

(c)

Fig. 1. (*continued*).

Table 1
Ionic radius mismatch (D_r) between Ca^{2+}/Li^+ and Tb^{3+} ions at different coordination numbers (CN), calculated using Shannon's effective ionic radii where R_m represent the ionic radii of the host cation and the dopant ion, respectively. A D_r value below 30% indicates favorable substitution with minimal lattice strain.

	Ca		Tb			Li		Tb	
D_r	R_m	CN	R_m	CN	D_r	R_m	CN	R_m	CN
7.7	1.00	6	0.923	6	64.08	0.675	5	0.923	6
D_r	R_m	CN	R_m	CN	D_r	R_m	CN	R_m	CN
7.54	1.06	7	0.98	7	21.44	0.76	6	0.923	6

Table 2
Rietveld-refined lattice parameters, unit cell volume, and reliability factors (R_p, R_{wp}, and R_{exp}) for undoped and Tb^{3+}-doped LiCBO phosphors with and without alkali-metal co-doping.

LiCBO						
Unit cell	Undoped	$0.03Tb^{3+}$	$0.05Tb^{3+}$	$0.07\ Tb^{3+}$	$0.05Tb^{3+}$,$0.01\ K^+$	$0.05Tb^{3+}$,$0.01Na^+$
a [Å]	6.08	6.08	6.08	6.08	6.08	6.08
b [Å]	13.2	13.28	13.28	13.28	13.28	13.28
c [Å]	6.18	6.1	6.18253	6.18	6.18	6.18
α,β,γ [°]	90,90,90	90,90,90	90,90,90	90,90,90	90,90,90	90,90,90
Vol. [Å^3]	499.3776	499.227	499.7276	499.7501	499.3349	499.45
χ^2	4.236	4.183	4.354	4.304	4.285	4.316
R_p	0.113	0.111	0.111	0.109	0.110	0.111
R_{wp}	0.169	0.167	0.174	0.173	0.172	0.173
R_{exp}	0.040	0.040	0.040	0.040	0.040	0.040

due to its different weighting of peak breadth and better handling of anisotropic broadening [44,49]. Compared to the Williamson–Hall model, the Halder–Wagner analysis yields slightly lower strain values, indicating that anisotropic strain components are effectively mitigated by monovalent ion incorporation.

The size–strain plot (Fig. 2d) provides a consolidated description of microstructural evolution, demonstrating a clear inverse correlation between crystallite size and lattice strain. As also seen in other nanoparticle and phosphor systems, larger crystallites are associated with lower microstrain and reduced dislocation density, reflecting fewer defect-related non-radiative centers [50,51]. The co-doped samples exhibit simultaneously larger crystallite sizes and reduced strain, highlighting the stabilizing role of Li^+/Na^+ ions in relieving defect-induced lattice stress.

Quantitative crystallite sizes and strain parameters derived from all models are summarized in Table 3. The crystallite size increases from ~60 nm (undoped) up to nearly 90 nm ($0.05Tb^{3+}$–$0.01\ K^+$, size–strain model), while the corresponding strain and dislocation density parameters decrease, comparable in magnitude ($\varepsilon \sim 10^{-3}$) to values reported for other RE-doped oxides and borates [51,52]. The consistency across different analytical approaches confirms that alkali-metal-assisted charge compensation not only enhances crystallinity but also suppresses excessive strain accumulation. Such microstructural optimization—larger grains, lower strain and dislocation density—is known to improve phonon management and suppress non-radiative losses, thereby supporting thermally stable Tb^{3+} emission in co-doped phosphor systems.

3.3. Morphological and compositional analysis (SEM–EDS)

The surface morphology of undoped and Tb^{3+}-doped LiCBO samples was examined by scanning electron microscopy (SEM), and the corresponding micrographs are shown in Fig. 3(a,b). The undoped LiCBO sample exhibits an irregular and porous morphology composed of agglomerated grains with non-uniform sizes, indicating limited grain coalescence during synthesis. The surface appears relatively rough, with loosely packed primary particles distributed throughout the microstructure. Upon Tb^{3+} incorporation (LiCBO:$0.05Tb^{3+}$), a clear modification in morphology is observed (Fig. 3b). The grains become more compact and better interconnected, forming a denser microstructure with reduced porosity. Although some degree of agglomeration remains, the overall surface homogeneity is improved compared to the undoped sample. This morphological densification is consistent with the enhanced crystallinity inferred from XRD peak-broadening analyses.

The elemental composition of the samples was analyzed using energy-dispersive X-ray spectroscopy (EDS). The detected elements (Li*, Ca, Tb, B*, and O) are consistent with the nominal composition of the host lattice, confirming the successful incorporation of Tb^{3+} ions without extraneous impurities, where the asterisks denote low-Z elements with inherently weak EDS signals. The absence of foreign elemental peaks further supports the phase purity inferred from the XRD results. Overall, the SEM–EDS analyses demonstrate that Tb^{3+} incorporation leads to a more compact microstructure while preserving compositional integrity. Such microstructural stabilization is expected to limit defect-related scattering centers, reducing non-radiative recombination/defect-related quenching centers in the lattice, and provides a structurally reliable basis for the optical investigations discussed in the subsequent sections.

Given that the synthesized LiCBO:Tb^{3+} samples form homogeneous bulk polycrystalline powders without engineered nanoscale heterostructures, the combination of Rietveld-refined XRD, FTIR/Raman and SEM–EDS analyses was considered sufficient for structural and microstructural characterization within the scope of this study.

3.4. Vibrational analysis (FTIR and Raman)

The vibrational characteristics of undoped and Tb^{3+}/alkali co-doped LiCBO samples were investigated by FTIR and Raman spectroscopy to elucidate the evolution of the borate network upon substitution.

The FTIR spectra (Fig. 4a) exhibit characteristic absorption bands associated with borate structural units. The strong bands located at ~1438 and ~ 1203 cm^{-1} are attributed to the asymmetric stretching vibrations of trigonal BO_3 units, while the features in the 918–755 cm^{-1} region correspond to stretching modes of tetrahedral [BO_4] groups, in agreement with typical BO_3 (1200–1600 cm^{-1}) and BO_4 (800–1200 cm^{-1}) assignments reported for borate-based materials and borate networks [53–55]. The low-frequency bands around ~636 and ~ 510 cm^{-1} are assigned to B–O–B bending vibrations, consistent with previous

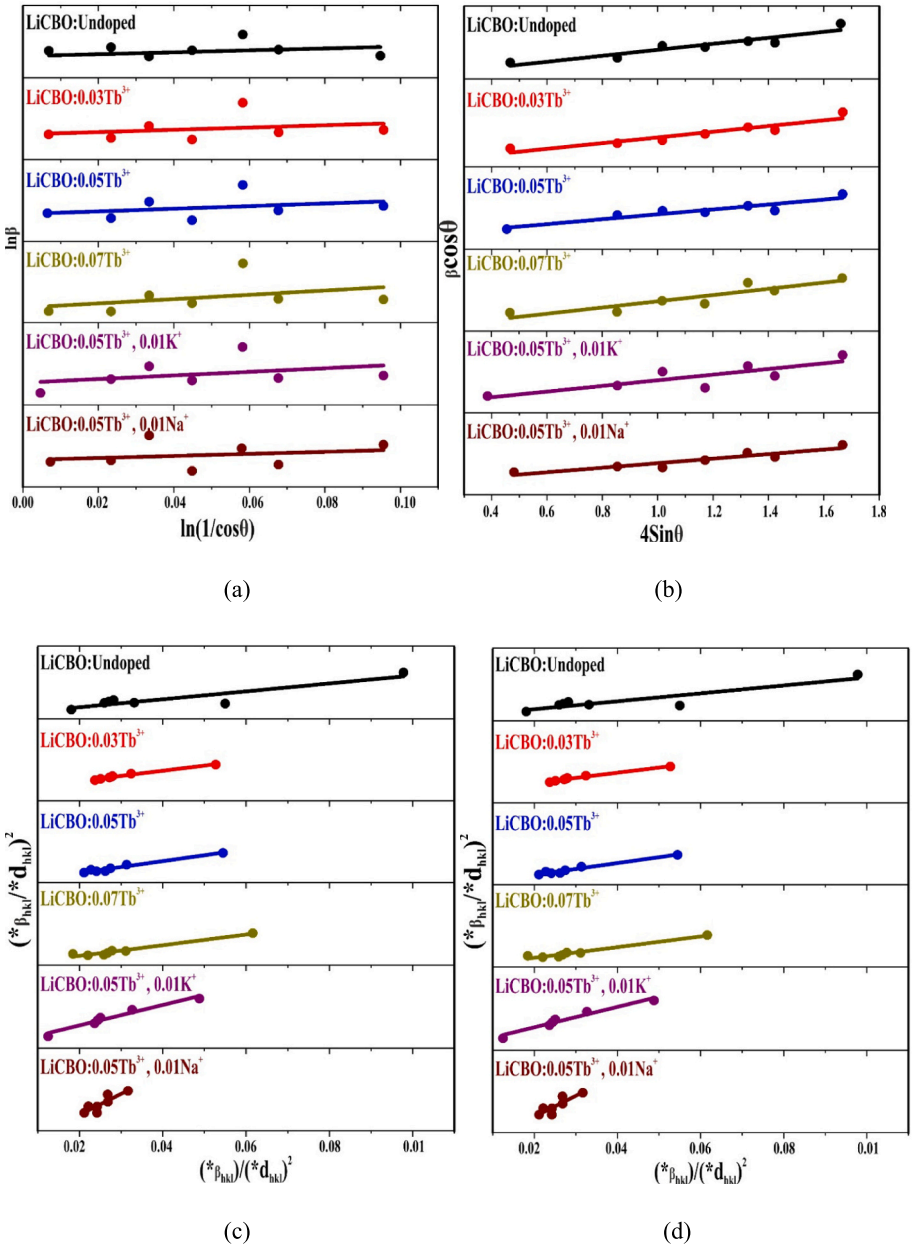

Fig. 2. XRD peak broadening-based crystallite size and lattice strain analysis of Tb^{3+}-doped and alkali co-doped LiCBO phosphors using (a) Monshi–Scherrer, (b) Williamson–Hall, (c) Halder–Wagner, and (d) size–strain plot approaches.

Table 3
Microstructural parameters (average crystallite size, lattice strain, and related defect indicators) of Tb^{3+}-doped and alkali co-doped LiCBO phosphors obtained from Monshi–Scherrer, Williamson–Hall, Halder–Wagner, and size–strain plot models.

Concentration		Undoped	0.03Tb^{3+}	0.05Tb^{3+}	0.07 Tb	0.05Tb^{3+},0.01 K^{+}	0.05Tb^{3+},0.01Na^{+}
Debye-Scherer	D (nm)	60.359	64.573	69.147	69.777	79.080	75.440
	$\delta \times 10^{-3}$ (nm^{-2})	0.274	0.239	0.209	0.205	0.159	0.175
Monshi-Scherrer	D (nm)	64.027	67.448	71.121	76.588	79.758	75.362
	$\delta \times 10^{-3}$ (nm^{-2})	0.243	0.219	0.197	0.170	0.157	0.176
Williamson-Hall	D (nm)	59.350	69.959	72.408	75.820	77.858	74.264
	$\varepsilon \times 10^{-3}$	2.36	2.25	1.77	2.24	2.42	1.15
Halder-Wagner	D (nm)	59.523	66.225	68.493	71.942	79.365	71.942
	$\varepsilon \times 10^{-3}$	24.74	11.82	12.08	12.03	10.58	10.11
Size-strain	D (nm)	61.362	69.290	76.219	80.903	89.392	76.219
	$\varepsilon \times 10^{-3}$	2.55	2.41	2.02	1.53	1.27	1.12

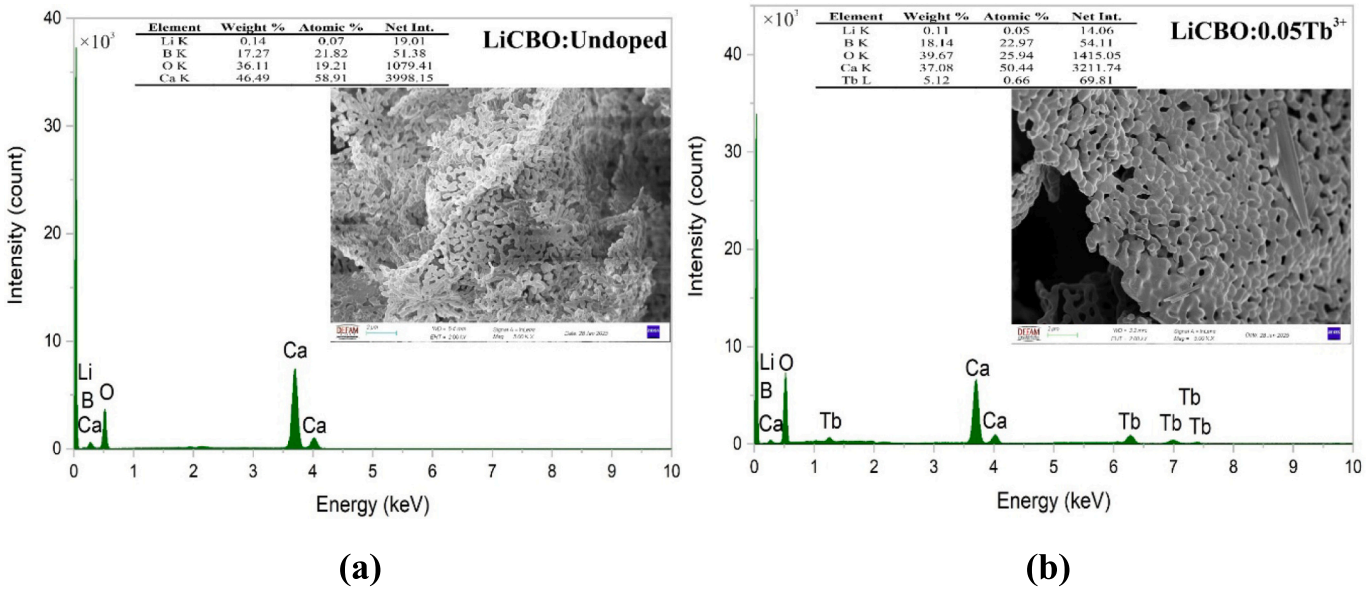

Fig. 3. (a) SEM micrograph of undoped LiCBO showing an irregular and porous morphology with agglomerated grains; the corresponding EDS elemental analysis is included within the image. (b) SEM micrograph of Tb^{3+}-doped LiCBO (LiCBO:0.05Tb^{3+}) exhibiting a more compact and interconnected microstructure; the embedded EDS results confirm the presence of Tb together with the host elements.

borate network analyses [53,56]. The coexistence of BO_3 and BO_4 units confirms the mixed borate framework of LiCBO. Upon Tb^{3+} doping and alkali-metal co-doping, no additional vibrational modes emerge; however, small but systematic band shifts (on the order of a few cm^{-1} toward higher wavenumber for BO_4-related bands) and slight broadening of the BO_3/BO_4 envelopes are observed, indicating local structural distortion and modification of bond force constants rather than a change in the fundamental borate network topology [57].

Raman spectra (Fig. 4b) further corroborate these observations. Prominent Raman bands near ~919 cm^{-1} are associated with symmetric stretching of BO_4 units, whereas modes in the 1500–1700 cm^{-1} range originate from B—O stretching vibrations in BO_3 groups, in line with reported Raman signatures of borate networks [58,59]. The bands observed between ~1890 and 2020 cm^{-1} are attributed to overtone and combination bands of the fundamental borate vibrations, linked to higher-order borate network connectivity [56. With increasing Tb^{3+} concentration and alkali co-doping, the normalized intensity ratio I(BO_4)/I(BO_3) exhibits a slight increase, suggesting a subtle $BO_3 \rightarrow BO_4$ conversion driven by charge-compensation-induced network rearrangement associated with the modifier-like behavior of alkali ions, similar to $BO_3 \rightarrow BO_4$ transformations reported upon modifier addition in other borate systems [60].

Importantly, the absence of additional Raman or FTIR bands confirms that Tb^{3+} and alkali ions are incorporated into the LiCBO lattice without forming secondary phases. The combined FTIR–Raman analysis shows that charge-compensated Tb^{3+} incorporation induces localized distortion and network reorganization while preserving the overall borate framework. This controlled modulation of the short-range order is expected to tune the local crystal field around Tb^{3+} ions, thereby affecting radiative transition probabilities and enhancing the thermal stability of the luminescence.

4. PL measurements

4.1. Room-temperature photoluminescence excitation and emission characteristics of Tb^{3+} in $LiCa_4O(BO_3)_3$

The room-temperature photoluminescence excitation (PLE) and emission (PL) properties of LiCBO: Tb^{3+} phosphors were systematically investigated to elucidate the excitation pathways, emission behavior, and concentration-dependent luminescence evolution. Fig. 5(a) presents the excitation and emission spectra of a representative LiCBO:0.005Tb^{3+} sample, while Fig. 5(b) illustrates the evolution of emission spectra as a function of Tb^{3+} concentration under near-UV excitation.

The excitation spectrum monitored at 542 nm exhibits several sharp bands in the 230–380 nm region, which are assigned to intra-$4f^8 \rightarrow 4f^8$ transitions of Tb^{3+} originating from the $^7F_6$ ground state to higher-lying $^5D_3$, $^5D_4$, and ^5G_j levels [11,61,62]. This kind of narrow 4f–4f excitation structure is typical for rare-earth-ion-doped phosphors, where the shielded 4f orbitals give rise to parity-forbidden but spectrally sharp transitions largely insensitive to the host lattice [63]. The intense excitation bands centered around ~238, 268, 302, 316, and 377 nm confirm that the Tb^{3+}-activated LiCBO phosphor can be efficiently excited by near-UV light sources, making it compatible with commercially available NUV-LED chips [64,65]. The absence of a broad charge-transfer band and the dominance of sharp 4f–4f lines indicate that the excitation is governed by direct 4f–4f transitions rather than host-to-activator charge-transfer processes, in agreement with the general behavior of Tb^{3+} in oxide and borate hosts [62]. Moreover, borate-based hosts such as LiCBO are known for low phonon energies and wide optical transparency, which support efficient radiative recombination of rare-earth ions under UV/NUV excitation [65].

The excitation wavelength of 377 nm was selected because it coincides with one of the intense 4f–4f absorption bands observed in the PLE spectrum of Tb^{3+} in LiCBO (Fig. 5a), ensuring efficient population of the $^5D_4$ emitting level. Moreover, 377 nm lies within the typical emission range of commercially available near-UV LED chips (365–405 nm), which are commonly employed for pumping Tb^{3+}-activated green phosphors. Therefore, the chosen excitation wavelength is representative of practical NUV-LED excitation conditions and relevant for evaluating the application potential of LiCBO:Tb^{3+} phosphors. Upon excitation at 377 nm, the emission spectrum is dominated by a series of sharp lines characteristic of Tb^{3+} transitions from the $^5D_4$ excited state to the ^7F_j ($J = 6$–0) manifold [66]. Among these, the intense green emission at ~542 nm corresponding to the $^5D_4 \rightarrow {}^7F_5$ transition is the most prominent, accompanied by weaker emissions at ~488 nm ($^5D_4 \rightarrow {}^7F_6$), ~584 nm ($^5D_4 \rightarrow {}^7F_4$), ~621 nm ($^5D_4 \rightarrow {}^7F_3$), and ~ 652–680 nm ($^5D_4 \rightarrow {}^7F_{2,1,0}$) [62] Such intense green $^5D_4 \rightarrow {}^7F_j$ emission bands of Tb^{3+}, especially the dominant $^5D_4 \rightarrow {}^7F_5$ line near 540 nm, are a hallmark of Tb^{3+}-activated phosphors and are widely exploited for high-purity green

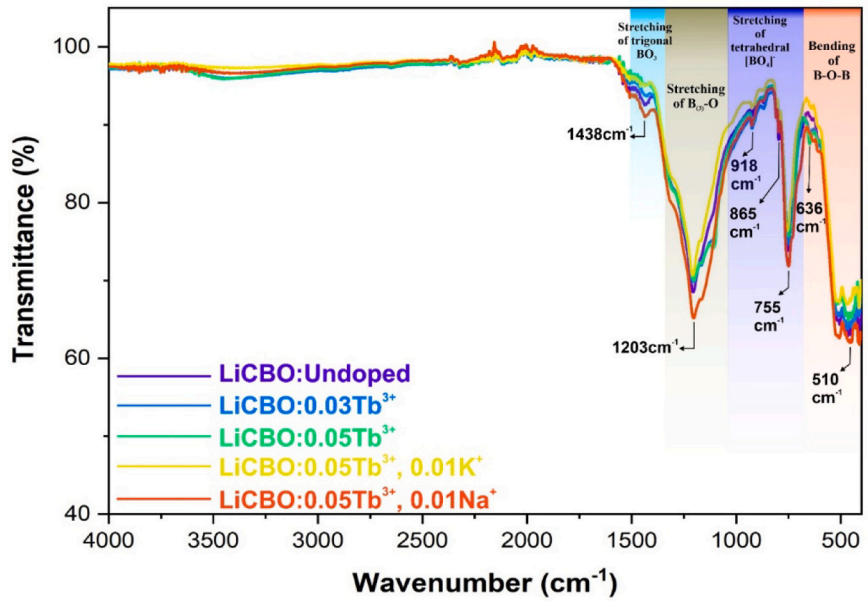

(a)

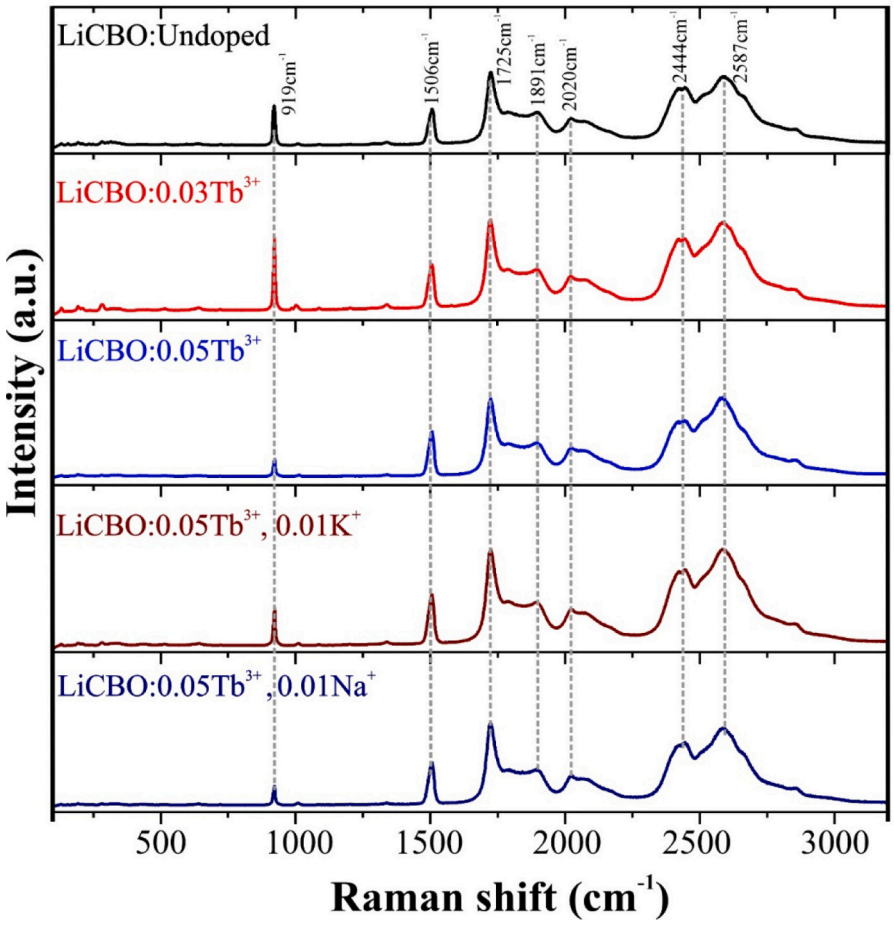

(b)

Fig. 4. (a) FTIR spectra of undoped, Tb^{3+}-doped, and alkali-metal co-doped LiCBO samples recorded in the 400–4000 cm^{-1} range, showing characteristic vibrational bands of trigonal BO_3 and tetrahedral BO_4 structural units. (b) Raman spectra of undoped and doped LiCBO samples illustrating the evolution of borate network vibrations upon Tb^{3+} incorporation and alkali-metal co-doping.

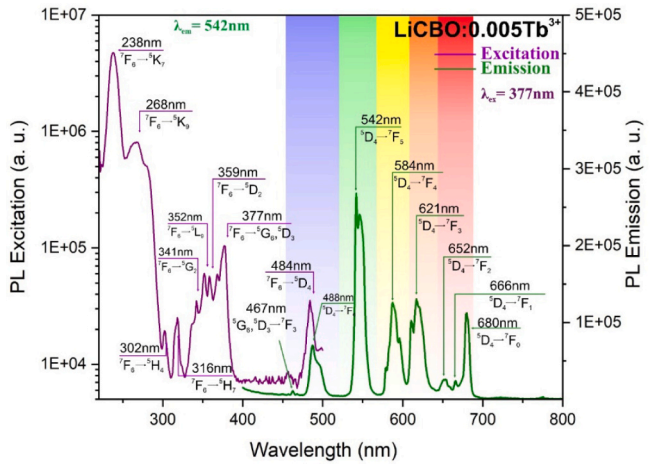

(a)

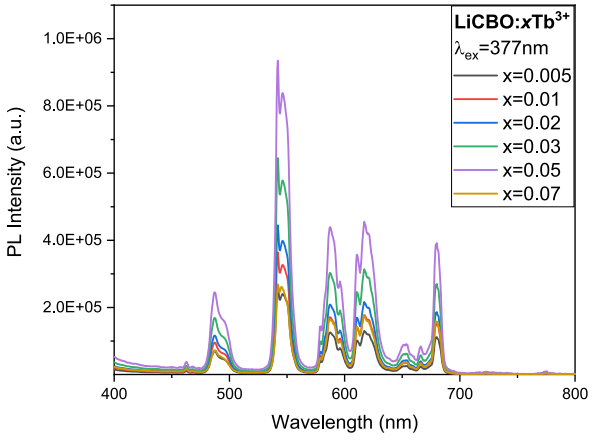

(b)

Fig. 5. Room-temperature photoluminescence properties of LiCBO:Tb^{3+} phosphors: (a) excitation and emission spectra of LiCBO:0.005Tb^{3+} monitored at λ_{em} = 542 nm and λ_{ex} = 377 nm, respectively; (b) concentration-dependent emission spectra of LiCBO:xTb^{3+} (x = 0.005–0.07) under near-UV excitation, showing maximum green emission at x = 0.05 followed by concentration quenching. (For interpretation of the references to color in this figure legend, the reader is referred to the web version of this article.)

emission in lighting and display applications. The dominance of the magnetic-dipole-allowed $^5D_4 \rightarrow {}^7F_5$ transition indicates a relatively low-symmetry local environment around Tb^{3+} ions, consistent with their preferential substitution at Ca^{2+} sites in the LiCBO lattice, as supported by ionic radius analysis and structural modeling for Tb^{3+} in LiCBO. The sensitivity of Tb^{3+} emission intensity and branching ratios to local crystal field symmetry is well established and directly links site occupation and symmetry to radiative versus non-radiative relaxation [67].

Fig. 5(b) reveals a pronounced dependence of emission intensity on Tb^{3+} concentration. With increasing Tb^{3+} content, the green emission intensity increases steadily and reaches a maximum at x = 0.05. The optimal Tb^{3+} concentration of x = 0.05 (≈ 5 wt%) is relatively high compared with many Tb^{3+}-activated phosphors, indicating that the LiCBO host can accommodate a substantial amount of Tb^{3+} ions before the onset of concentration quenching. This behavior suggests efficient spatial separation of activator sites and a rigid, low-phonon-energy borate framework that suppresses non-radiative energy migration to quenching centers. Further increase in activator concentration leads to a gradual decrease in emission intensity, indicating the onset of concentration quenching beyond this optimal level. Such concentration-dependent behavior, with an optimum Tb^{3+} content followed by quenching, is commonly observed in Tb^{3+}-doped borate and phosphate hosts and is attributed to enhanced Tb^{3+}–Tb^{3+} interactions at higher doping levels. The quenching behavior is attributed to enhanced non-radiative energy transfer among neighboring Tb^{3+} ions through cross-relaxation and multipolar interactions, facilitated by the reduced average interionic distance at higher doping levels, in agreement with defect and interaction–driven concentration quenching mechanisms discussed for Tb^{3+} phosphors in related borate hosts [68]. The optimal Tb^{3+} concentration of $x = 0.05$ therefore represents a balance between efficient radiative emission and minimized non-radiative losses.

Additional emission spectra recorded under alternative excitation wavelengths (238, 268, 302, 316, and 352 nm), although not shown here for brevity, exhibit identical spectral profiles dominated by the $^5D_4 \rightarrow {}^7F_5$ transition. The invariance of emission peak positions and relative line intensities across different excitation wavelengths confirms that the luminescence originates from the same emitting $^5D_4$ level, independent of the initial excitation channel. This excitation-wavelength-insensitive behavior is consistent with the general property of 4f–4f transitions in rare-earth ions, which remain largely unaffected by external perturbations due to the shielding of 4f electrons. Notably, excitation through higher-energy 4f levels results in comparable concentration-dependent trends, with maximum emission consistently observed at x = 0.05, reinforcing the intrinsic nature of the observed quenching mechanism.

Overall, the PLE–PL analyses demonstrate that LiCBO provides a structurally stable and optically efficient host for Tb^{3+} activation. This behavior aligns with the broader understanding that borate lattices, with rigid BO_3 frameworks and low phonon energies, offer chemically and thermally stable platforms that favor radiative recombination of rare-earth ions and support efficient Tb^{3+} green emission over a wide temperature range. The combination of strong near-UV excitation, intense green emission with high color purity, and a well-defined optimal activator concentration highlights the suitability of LiCBO:Tb^{3+} phosphors for green-emitting solid-state lighting applications.

Using the critical distance model, the energy transfer mechanism among Tb^{3+} ions in LiCBO was evaluated. For the present system, the critical concentration was determined as $x_c = 0.05$, corresponding to the maximum emission intensity. Considering that Tb^{3+} ions substitute Ca^{2+} sites, and that the LiCBO unit cell contains 16 available Ca sites (Z = 4), the critical distance was calculated using the Blasse equation based on Dexter-type concentration quenching theory [69]. With a unit-cell volume of 499.73 $Å^3$, the critical distance was estimated to be $R_c \approx 10.6$ Å. Since this value is significantly larger than the typical 3–5 Å range required for exchange interaction, exchange interaction can be excluded, indicating that the concentration quenching mechanism is governed by electric multipolar interactions, most likely of the electric dipole–dipole type, as also reported for Tb^{3+}–Tb^{3+} and Tb^{3+}–Ln^{3+} systems in various borate and oxide hosts [70,71].

4.2. *Effect of alkali-metal co-doping on Tb^{3+} emission behavior*

The influence of alkali-metal co-doping on the photoluminescence performance of LiCBO:0.05Tb^{3+} was systematically investigated by introducing K^+ and Na^+ ions, and the corresponding emission spectra under 377 nm excitation are presented in Fig. 6(a,b). For both co-doping series, a pronounced enhancement of the Tb^{3+}-related green emission is observed compared to the alkali-free reference sample, with the emission intensity increasing by nearly one order of magnitude at the optimal alkali-ion concentration [23,26].

In the absence of alkali ions, Tb^{3+} substitutes Ca^{2+} sites in the LiCBO lattice, leading to local charge imbalance and defect formation, such as cation vacancies or distorted coordination polyhedra, which act as non-radiative recombination centers, analogous to other non-equivalent rare-earth substitutions in oxide and borate hosts [72,73]. Upon alkali co-doping, monovalent K^+/Na^+ ions compensate the excess positive

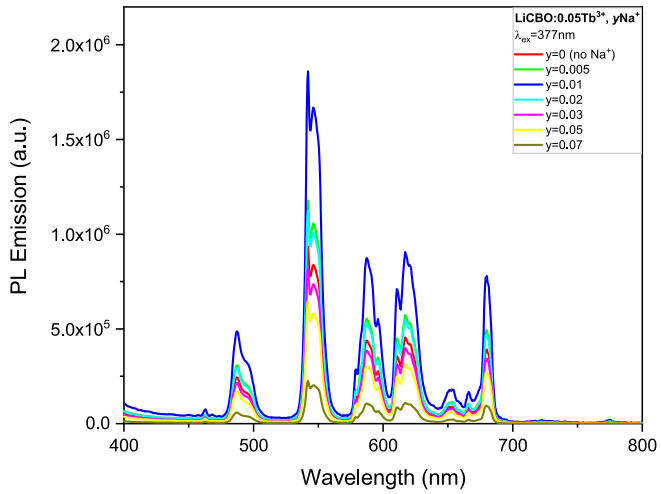

(a)

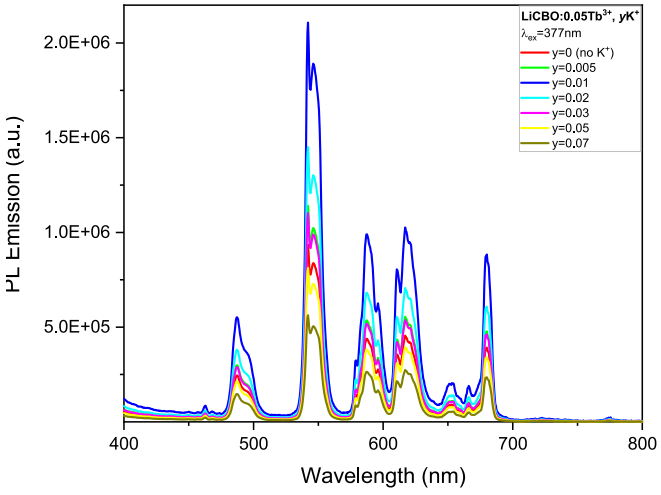

(b)

Fig. 6. Emission spectra of LiCBO:0.05Tb^{3+} phosphors co-doped with (a) Na^+ and (b) K^+ under 377 nm excitation, showing pronounced enhancement of Tb^{3+} green emission at the optimal alkali concentration ($y = 0.01$) followed by concentration quenching at higher dopant levels. (For interpretation of the references to color in this figure legend, the reader is referred to the web version of this article.)

charge and modify the local Tb—O environment, thereby suppressing defect-assisted non-radiative pathways and tuning the crystal-field symmetry around Tb^{3+}, consistent with charge-compensation–driven enhancement reported for alkali co-doped Tb^{3+}/Eu^{3+} phosphors [74]. Under 377 nm excitation, alkali co-doping markedly enhances the Tb^{3+} green emission in LiCBO:0.05Tb^{3+} (Fig. 6(a) and (b)). For Na^+ co-doping, the integrated emission intensity rises by ~2.0× and reaches a maximum at $y = 0.01$, after which concentration quenching occurs. K^+ co-doping produces a slightly larger enhancement of ~2.25× at the same optimal content ($y = 0.01$), which is attributed to its larger ionic radius and higher polarizability that enable more effective modulation of the Tb^{3+} crystal field. Notably, inspection of the emission spectra reveals no measurable shift in the $^5D_4 \rightarrow {}^7F_j$ peak positions, confirming that the intrinsic 4f–4f transitions remain unaffected; however, K^+ co-doping induces a more pronounced redistribution of relative peak intensities compared to Na^+, indicative of a stronger reduction in local site symmetry and enhanced crystal-field asymmetry around Tb^{3+} ions [75,76]. The achieved enhancement factors fall within the typical few- to ten-fold range reported for alkali co-doped rare-earth phosphors, including Tb^{3+}-activated $LiSrVO_4$ and $K_7SrY_2(B_5O_{10})_3$ as well as Eu^{3+}-activated $GdPO_4$ and $Ba_5P_6O_{20}$ hosts, where 2–12× photoluminescence gains are commonly observed upon $Li^+/Na^+/K^+$ co-doping [23,37,72. The strong intensity gain (approaching an order of magnitude) points to a substantial reduction of non-radiative relaxation rates rather than a mere increase in absorption probability, in line with lifetime-based evidence of reduced non-radiative losses in alkali co-doped Tb^{3+}/Eu^{3+} systems. Although our measurements do not directly probe lattice dynamics, the observed behavior is consistent with the above charge-compensation and defect-suppression mechanism. Such behavior closely parallels alkali charge-compensated Tb^{3+} and Eu^{3+} phosphors in vanadate, phosphate and borate hosts, reinforcing that the dominant role of K^+/Na^+ is to restructure the defect landscape and local symmetry rather than to alter the intrinsic Tb^{3+} 4f energy levels [23,26,74]. At higher alkali concentrations, a gradual decrease in emission intensity is observed, indicating the onset of concentration quenching. This behavior is attributed to enhanced energy migration among Tb^{3+} ions facilitated by increased structural connectivity, ultimately leading to non-radiative energy loss via multipolar interactions. The existence of a well-defined optimum alkali concentration therefore reflects a balance between activation by alkali-induced charge compensation and concentration-driven quenching.

Overall, the results presented in Fig. 6 demonstrate that alkali-metal co-doping is a highly effective strategy for amplifying Tb^{3+} emission in LiCBO phosphors. The substantial intensity enhancement highlights the critical role of charge-compensated lattice engineering in optimizing radiative efficiency and underscores the potential of alkali-assisted Tb^{3+}-activated borate phosphors for high-performance green-emitting photonic applications [77].

4.3. *High-temperature photoluminescence behavior of alkali-metal co-doped LiCBO:Tb^{3+}*

To evaluate the thermal robustness of LiCBO:0.05Tb^{3+} for high-power LED operation, temperature-dependent photoluminescence (PL) measurements were carried out in the 300–550 K range. Such an extended temperature window is representative of the junction temperatures typically encountered in high-power near-UV LED packages. Fig. 7(a) displays the PL emission spectra recorded at different temperatures under identical excitation conditions. Notably, the overall spectral profile remains unchanged throughout the entire temperature range, and no observable shift in the characteristic $^5D_4 \rightarrow {}^7F_j$ emission peak positions is detected. This spectral invariance indicates that the local coordination environment and crystal-field symmetry of Tb^{3+} ions are essentially preserved upon heating, thereby ruling out thermally induced phase transitions or changes in the crystallographic site occupation of Tb^{3+}. The thermal quenching behavior was quantitatively evaluated by tracking the integrated intensity of the dominant green emission band at 542 nm ($^5D_4 \rightarrow {}^7F_5$), normalized as I(T)/I(300*K*), as shown in Fig. 7(b). With increasing temperature, the emission intensity gradually decreases, retaining approximately 40–45% of its initial value in the 423–450 K range. At higher temperatures, a minimum intensity is observed around 500 K, followed by a partial recovery at 550 K. The partial re-entrant behavior at the highest temperature suggests a reversible thermal population redistribution among the Tb^{3+} Stark sublevels and/or thermally activated trapping–detrapping processes involving shallow defect states, rather than irreversible structural degradation of the host lattice. At elevated temperatures, additional thermally assisted carrier redistribution processes may become competitive with the dominant non-radiative multiphonon relaxation channel. In particular, shallow defect levels associated with charge-compensation-related lattice imperfections can act as temporary carrier reservoirs. Thermal detrapping from these defect states can partially repopulate the Tb^{3+} $^5D_4$ emitting level, giving rise to the observed non-

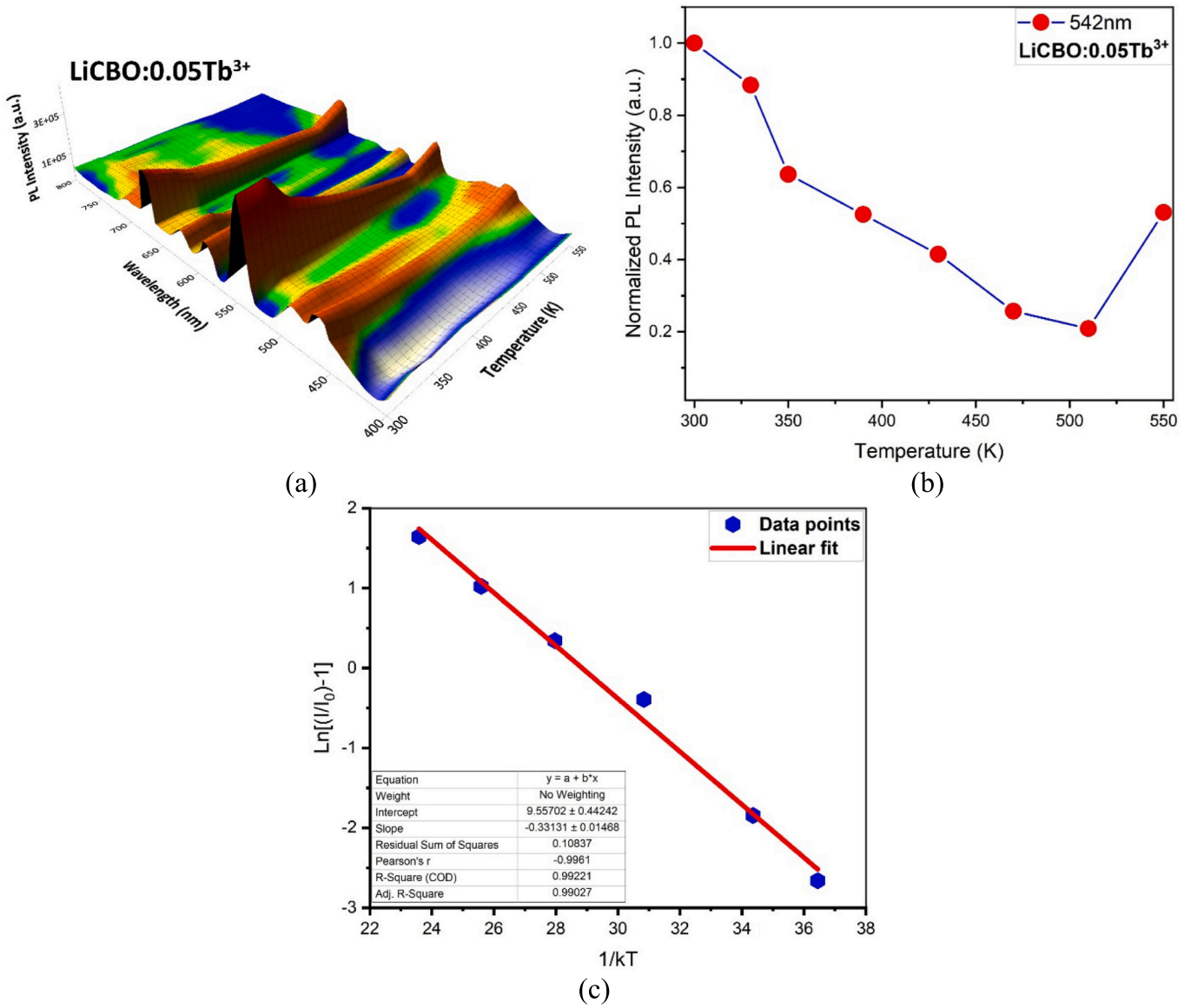

Fig. 7. (a) Temperature-dependent three-dimensional photoluminescence (PL) emission map of LiCBO:0.05Tb^{3+} recorded between 300 and 550 K under 377 nm excitation. (b) Normalized PL intensity of the $^5D_4 \rightarrow {}^7F_5$ emission at 542 nm as a function of temperature. (c) Linearized thermal quenching behavior of the 542 nm emission used to extract the activation energy.

monotonic intensity recovery above ~500 K. Such competing radiative and non-radiative pathways are commonly reported in rare-earth-doped oxide and borate phosphors operating in extended high-temperature regimes. Similar non-monotonic temperature dependences associated with Tb^{3+}-related trapping processes have been reported in other oxide and borate phosphors [63,78].

To gain further insight into the non-radiative relaxation mechanism, the temperature dependence of the PL intensity was analyzed using an Arrhenius-type model. The linear relationship observed in the $\ln[(I_0/I) - 1]$ versus $1/kT$ plot (Fig. 7(c)) within the primary quenching regime (300–450 K) indicates the presence of a dominant thermally activated non-radiative channel in this temperature range. From the slope of the linear fit, an activation energy of approximately $E_a \approx 0.33$ eV is extracted, which lies in the moderate-to-high range reported for Tb^{3+}-activated oxide and borate phosphors [79,80]. Such an activation barrier is sufficiently large to suppress thermally activated non-radiative pathways at typical LED junction temperatures (~400–450 K), ensuring that a substantial fraction of the excitation energy still decays radiatively under device-relevant operating conditions.

The observed thermal stability can be attributed to the combined effects of $Tb^{3+} \rightarrow Ca^{2+}$ heterovalent substitution and the intrinsically rigid, low-phonon-energy borate framework. The rigid borate network effectively suppresses multiphonon relaxation processes, thereby delaying the onset of thermal quenching and maintaining radiative efficiency at elevated temperatures. This behavior is consistent with previous studies on Tb^{3+}- and Eu^{3+}-doped borate and phosphate phosphors, where strong host rigidity was shown to improve thermal quenching resistance and maintain color stability at high temperatures [28,81]. As will be discussed in the following subsection, alkali-metal co-doping and the associated charge-compensation schemes can further modify defect populations and thermal quenching behavior.

Overall, these results demonstrate that LiCBO:0.05Tb^{3+} maintains stable green emission with significant intensity retention under high-temperature operating conditions relevant to near-UV-pumped solid-state lighting. The combination of spectral stability, moderate thermal quenching, and relatively high activation energy underscores the suitability of this Tb^{3+}-activated borate phosphor for high-power photonic applications such as high-brightness LEDs and other solid-state lighting

devices.

Following the analysis of the alkali-free LiCBO:0.05Tb^{3+} phosphor, the effect of alkali-metal co-doping on the high-temperature photoluminescence behavior was further examined using representative K^+- and Na^+-co-doped compositions ($y = 0.01$). Temperature-dependent PL emission spectra recorded between 300 and 550 K are shown in Figs. 8 (a) and 9(a). For both co-doped samples, the overall spectral profile and the characteristic $^5D_4 \rightarrow {}^7F_j$ emission peak positions remain unchanged upon heating, confirming that alkali co-doping preserves the host structure and local Tb^{3+} crystal field without inducing thermally driven phase transitions [28,78].

The thermal quenching behavior was quantitatively evaluated by tracking the normalized integrated intensity of the dominant 542 nm ($^5D_4 \rightarrow {}^7F_5$) emission band as a function of temperature, as presented in Figs. 8(b) and 9(b). Compared to the alkali-free phosphor, both K^+- and Na^+-co-doped samples exhibit higher absolute emission intensities over the entire temperature range while maintaining a similar I(T)/I(300 K) profile, consistent with alkali-assisted charge compensation and defect control reported in other oxide and borate hosts [82,83]. In both cases, the PL intensity decreases gradually with increasing temperature, reaches a minimum around 450–500 K, and partially recovers at higher temperatures, suggesting reversible thermal population redistribution among Tb^{3+} Stark sublevels and/or shallow-trap-assisted detrapping processes rather than irreversible lattice degradation, in agreement with

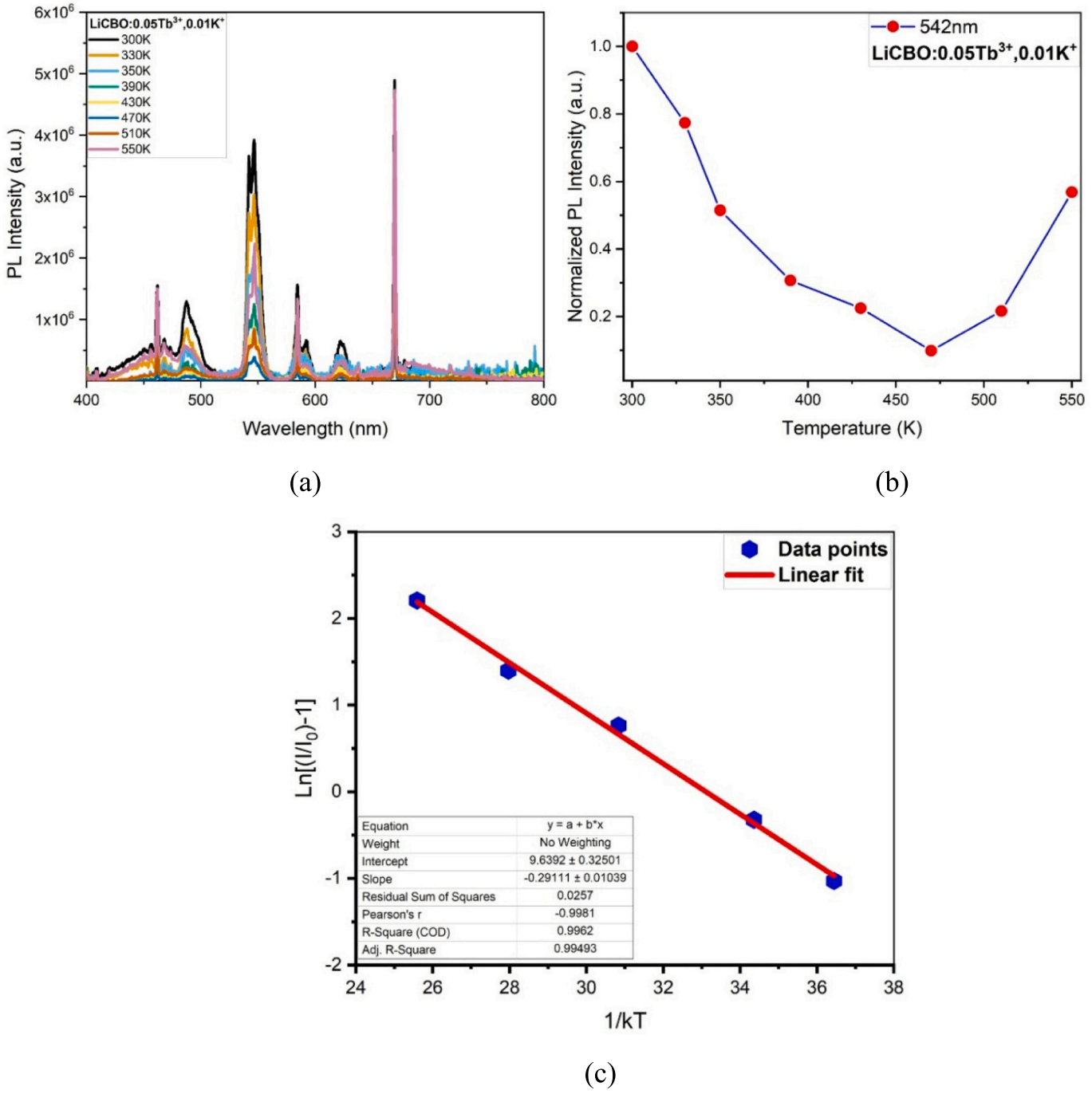

Fig. 8. (a) Temperature-dependent two-dimensional photoluminescence (PL) emission of LiCBO:0.05Tb^{3+}, 0.01 K^+ recorded between 300 and 550 K under 377 nm excitation. (b) Normalized PL intensity of the $^5D_4 \rightarrow {}^7F_5$ emission at 542 nm as a function of temperature. (c) Linearized thermal quenching behavior of the 542 nm emission used to extract the activation energy.

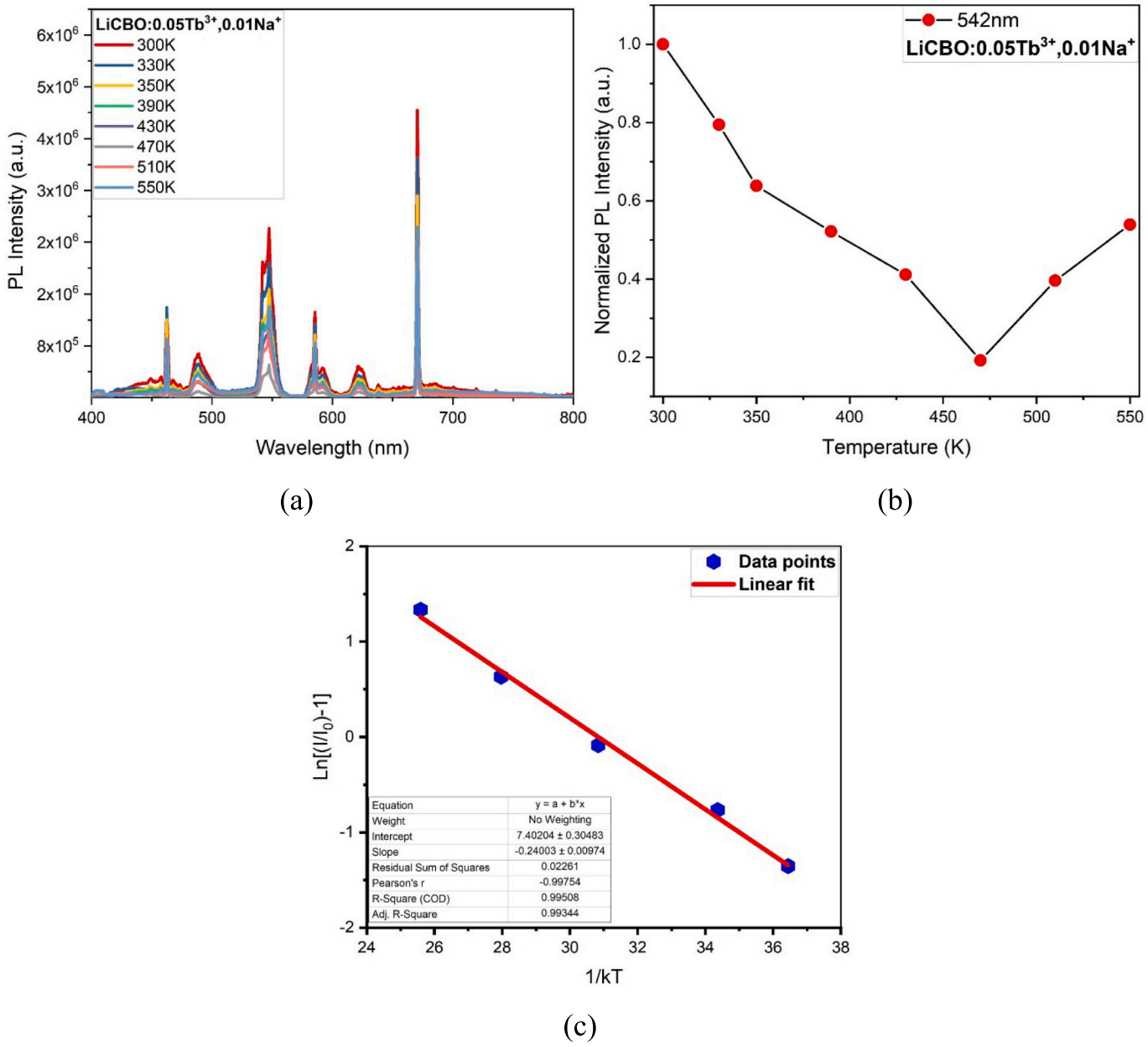

Fig. 9. (a) Temperature-dependent two-dimensional photoluminescence (PL) emission of LiCBO:0.05Tb^{3+}, 0.01Na^{+} recorded between 300 and 550 K under 377 nm excitation. (b) Normalized PL intensity of the $^5D_4 \rightarrow {}^7F_5$ emission at 542 nm as a function of temperature. (c) Linearized thermal quenching behavior of the 542 nm emission used to extract the activation energy.

previously observed Tb^{3+}-related trapping phenomena [23,84].

Further insight into the thermal quenching mechanism was obtained from Arrhenius analysis of the temperature-dependent PL intensity, as shown in Figs. 9(c) and 10(c). The extracted activation energies follow the trend E_a(alkali-free) > E_a(K^+) > E_a(Na^+), indicating that alkali co-doping slightly lowers the thermal barrier for non-radiative processes. Despite this reduction in E_a, alkali-ion charge compensation suppresses defect-related non-radiative recombination pathways relative to the alkali-free reference, leading to higher usable emission intensity and stable chromaticity under device-relevant operating temperatures, similar to other rare-earth phosphors where $Li^+/Na^+/K^+$ co-doping enhances PL via defect control [82,83].

The marginally higher activation energy and better thermal robustness observed for the K^+-co-doped LiCBO sample compared to its Na^+-co-doped counterpart are tentatively attributed to the larger ionic radius and higher polarizability of K^+, which can more effectively modulate the local defect landscape and crystal field around Tb^{3+} ions, as also suggested in K^+-modified borate and phosphate hosts. Overall, the results presented in Figs. 9 and 10 demonstrate that alkali-metal co-doping (particularly with K^+) optimizes the balance between charge compensation, defect suppression, and thermally activated processes, leading to enhanced high-temperature luminescence performance without compromising structural integrity or spectral stability, in line with the general behavior of alkali charge-compensated phosphors designed for high-power solid-state lighting.

4.4. Temperature-dependent FIR and relative sensitivity of alkali-metal co-doped LiCBO:Tb^{3+}

To further evaluate the thermometric potential of LiCBO:0.05Tb^{3+}, the temperature-dependent fluorescence intensity ratio (FIR) between the thermally responsive red emission at ~680 nm and the dominant

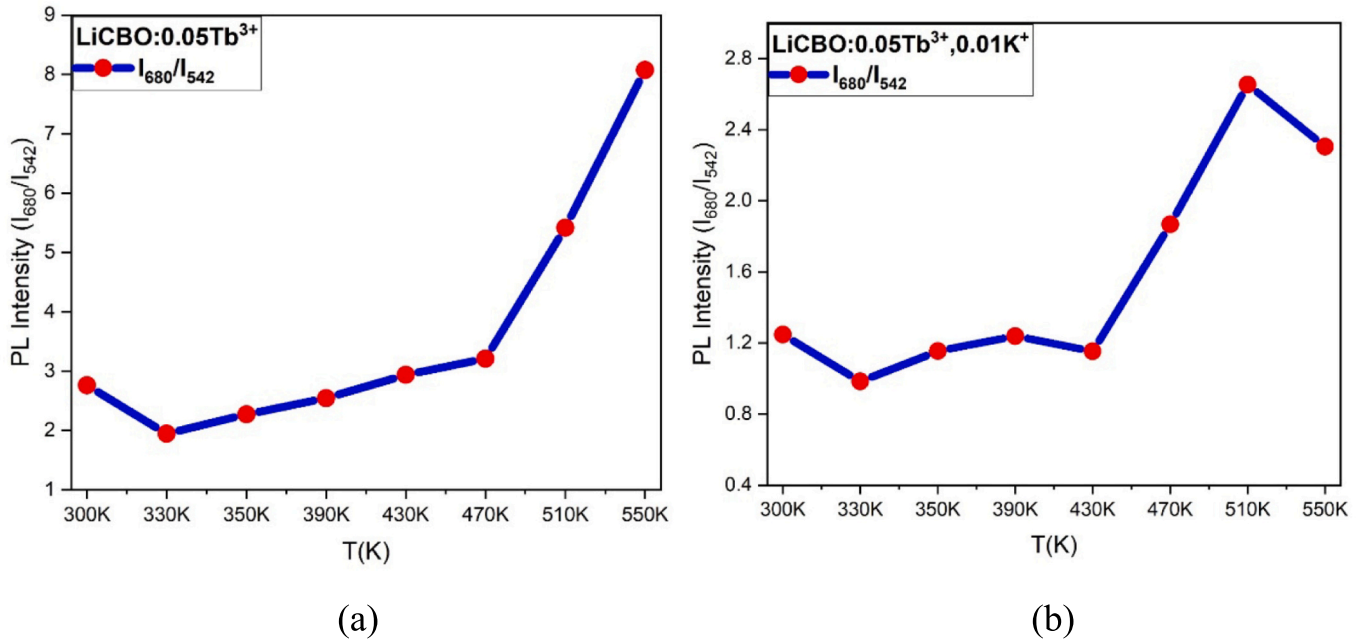

Fig. 10. Temperature dependence of the fluorescence intensity ratio (FIR = I_{680}/I_{542}) for (a) LiCBO:0.05Tb^{3+} and (b) LiCBO:0.05Tb^{3+}, 0.01 K^+ phosphors in the 300–550 K range, illustrating the thermally activated red-to-green emission ratio and its modulation by K^+ co-doping. (For interpretation of the references to color in this figure legend, the reader is referred to the web version of this article.)

green emission at 542 nm was analyzed over the 300–550 K range. The FIR was defined as FIR = I_{680}/I_{542}, where both bands originate from Tb^{3+} 4f–4f transitions but exhibit markedly different thermal responses [85].

As shown in Fig. 10(a), the FIR exhibits a gradual increase with temperature, followed by a pronounced enhancement above ~470 K, reflecting the thermally activated redistribution between the red and green Tb^{3+} emission channels. This behavior arises from the combined effects of gradual thermal quenching of the green $^5D_4 \rightarrow {}^7F_5$ transition and the thermally activated population of the red-emitting channels, leading to a rapid amplification of the FIR at elevated temperatures. The corresponding numerical FIR values and derived relative sensitivities are summarized in Table 4.

The relative sensitivity, calculated as

$$S_r = (1/FIR) \bullet (dFIR/dT)$$

shows a clear temperature dependence, with S_r increasing steadily and reaching a maximum value of approximately 1.3% K^{-1} around 500 K, which is comparable to or higher than many Tb^{3+}-based single-ion FIR thermometers. For instance, $Na_2Y_2TeB_2O_{10}$:Tb^{3+} has been reported to exhibit a maximum relative sensitivity of $S_{r,max} \approx$ 2.3–2.9% K^{-1} near 300 K based on excitation intensity ratio (EIR) thermometry, while significantly higher sensitivities were achieved using emission-based FIR models. [80]. In contrast, typical single-ion Tb^{3+} FIR thermometers in oxide and borate hosts generally exhibit $S_{r,max}$ values in the range of ≈0.4–1.3% K^{-1} over 300–550 K as summarized in recent literature [26,73]. Within this context, the $S_{r,max} \approx$ 1.3% K^{-1} observed for LiCBO:Tb^{3+} at ~500 K positions this phosphor among the higher-performing single-center Tb^{3+} thermometric systems operating at elevated temperatures. This sensitivity enhancement reflects an accelerated redistribution of excited-state populations at higher temperatures, where thermally assisted radiative pathways become increasingly competitive with non-radiative decay channels [86]. It should also be noted that higher sensitivities reported for Tb^{3+} single-band ratiometric (SBR) strategies are typically achieved under dual-excitation schemes and are therefore not directly comparable to the emission–emission FIR approach employed in this work.

Importantly, the FIR continues to increase monotonically above room temperature, while the relative sensitivity remains substantial over a broad high-temperature window (≈430–550 K). Such behavior is advantageous for practical optical thermometry, as it enables reliable temperature readout in the operational regime relevant to high-power near-UV-pumped devices [87]. The fact that both emission bands originate from the same Tb^{3+} activator further ensures intrinsic self-referencing, minimizing measurement errors caused by excitation power fluctuations or sample inhomogeneity.

To better benchmark the thermometric performance, Table 5 compares the present emission-based FIR thermometer (I_{680}/I_{542}) with a representative Tb^{3+} FIR system reported in a borate-related host. For $Na_2Y_2TeB_2O_{10}$:Tb^{3+}, markedly higher peak sensitivities ($S_{r,max}$ = 5.23–5.74%·K^{-1}) are obtained, but the maximum occurs at 300 K and the reported FIR operating window is limited to 300–475 K. In contrast, $LiCa_4O(BO_3)_3$:Tb^{3+} exhibits a competitive sensitivity of ~1.3%·K^{-1} in the elevated-temperature regime (~500 K) and remains operable up to 550 K, which is particularly relevant for high-temperature optical thermometry under near-UV LED operating environments.

Consistently, when compared with representative Tb^{3+} emission-based FIR thermometers reported in oxide and borate hosts (Table 5), it becomes evident that although higher peak sensitivities are often achieved near room temperature, the sensitivity in many systems decreases significantly at elevated temperatures. In contrast, the present LiCBO:Tb^{3+} phosphor maintains a competitive relative sensitivity (~1.3% K^{-1}) in the high-temperature region (~500 K) while preserving

Table 4
Temperature-dependent FIR and relative sensitivity of LiCBO:0.05Tb^{3+} with and without K^+ co-doping.

Temperature (K)	FIR (I_{680}/I_{542})-alkali free	S_r (% K^{-1}) alkali free	FIR (I_{680}/I_{542})- 0.01 K^+	S_r (% K^{-1})-0.01 K^+
300	2.76	–	1.25	–
330	1.95	0.74	0.98	0.62
350	2.27	0.46	1.15	0.48
390	2.55	0.36	1.22	0.34
430	2.94	0.33	1.16	0.29
470	3.22	0.40	1.85	0.56
510	5.44	1.28	2.63	1.05
550	8.06	0.97	2.30	0.82

Table 5
Benchmarking of Tb^{3+} emission-based FIR thermometers relevant to elevated-temperature operation.

Phosphor	Scheme	Emission ratio	Temperature range (K)	$S_{r,max}$ (%·K^{-1})	$T(S_{r,max})$ (K)	Ref.
$Na_2Y_2TeB_2O_{10}$:Tb^{3+} (NYTB:Tb^{3+})	FIR	I_{585}/I_{547}	300–475	5.74	300	[80]
$Na_2Y_2TeB_2O_{10}$:Tb^{3+} (NYTB:Tb^{3+})	FIR	I_{497}/I_{547}	300–475	5.23	300	[80]
$LiCa_4O(BO_3)_3$:0.05Tb^{3+} (this work)	FIR	I_{680}/I_{542}	300–550	≈1.3	≈500	This work

structural and spectral stability up to 550 K. This behavior suggests that the dominant thermometric mechanism in LiCBO:Tb^{3+} is governed by thermally assisted population redistribution between Stark sublevels of the $^5D_4$ state rather than defect-mediated non-radiative quenching, thereby enabling stable operation under high-power NUV-LED conditions. Overall, the combination of moderate sensitivity, extended temperature window, and smooth FIR response highlights the suitability of alkali-modulated LiCBO:Tb^{3+} phosphors for elevated-temperature optical sensing applications. Overall, the temperature-dependent FIR characteristics and the relatively high maximum sensitivity demonstrate that LiCBO:0.05Tb^{3+} is a promising single-ion phosphor for high-temperature luminescent thermometry. These performance metrics are comparable to or exceed those of several reported Tb^{3+}-activated thermometric phosphors operating in similar temperature ranges [23,85]. In the following section, the influence of alkali-metal co-doping on the FIR response and thermal sensitivity will be examined to assess whether charge-compensation-induced defects and lattice modifications can further tune the thermometric performance.

In addition to the alkali-free composition, the temperature-dependent fluorescence intensity ratio (FIR = I_{680}/I_{542}) was also evaluated for alkali co-doped LiCBO:0.05Tb^{3+}, focusing on the representative K^+-co-doped sample (0.01 K^+). As shown in Fig. 10(b) and summarized in Table 4, the FIR exhibits a clear temperature dependence over the 300–550 K range, increasing from ~1.2 at 300 K to a maximum of ~2.6 around 510 K, followed by a slight decrease at higher temperatures.

Compared to the alkali-free host, the absolute FIR values are reduced, indicating that K^+ co-doping partially suppresses the thermally activated red-to-green emission redistribution. In contrast to alkali co-doped systems where the primary outcome is an enhancement of thermometric sensitivity, the present K^+-modified LiCBO:Tb^{3+} phosphor prioritizes thermal stability and operational reproducibility over achieving the highest FIR amplitude [88]. For the 0.01 K^+ co-doped sample, the maximum relative sensitivity reaches $S_r,max \approx 1.05\%\ K^{-1}$ at around 510 K, which is slightly lower than that of the alkali-free composition ($S_{r,max} \approx 1.28\%\ K^{-1}$). Despite this moderate reduction in peak sensitivity, the FIR(T) response becomes noticeably smoother with reduced fluctuation amplitude, indicating enhanced thermal stability and improved reproducibility, which are advantageous for reliable optical thermometry. This trend is consistent with charge-compensation effects observed in other alkali-modified rare-earth phosphors, where alkali incorporation can reduce defect-assisted population channels and alter local crystal-field environments. Importantly, the FIR evolution remains smooth and reversible, confirming that alkali incorporation does not introduce additional thermally unstable non-radiative channels, in line with other Tb^{3+}- and Eu^{3+}-based systems where alkali co-doping improves thermal robustness.

Although the absolute FIR values in the K^+ co-doped sample are lower than those of the alkali-free composition, the FIR response exhibits improved thermal stability and reduced fluctuation over the entire temperature range. This behavior can be reasonably associated with K^+-induced charge compensation and partial lattice homogenization, which tend to stabilize the Tb^{3+} crystal-field environment and moderate defect-related thermal population pathways, similar to what has been reported for other alkali-co-doped borate, vanadate and phosphate hosts [26,73]. As a result, the FIR response in K^+-co-doped LiCBO:Tb^{3+} is smoother and more reproducible, which is advantageous for reliable optical thermometry.

4.5. Time-resolved luminescence decay analysis

The time-resolved luminescence decay behaviors of LiCBO:Tb^{3+} and alkali-ion (K^+ and Na^+) co-doped LiCBO:Tb^{3+} phosphors were investigated at room temperature. The decay curves recorded under identical excitation conditions are presented in Fig. 11 on a logarithmic scale. All samples exhibit pronounced non-single-exponential decay, revealing the presence of multiple recombination pathways and distinct local environments around Tb^{3+} centers, a behavior commonly observed in Tb^{3+}-activated borate and vanadate phosphors [89].

The experimental decay profiles were well fitted using a multi-exponential decay function expressed as:

$I(t) = \sum_i A_i exp\left(-\frac{t}{\tau_i}\right)$ where τ_i denotes the decay lifetimes and A_i

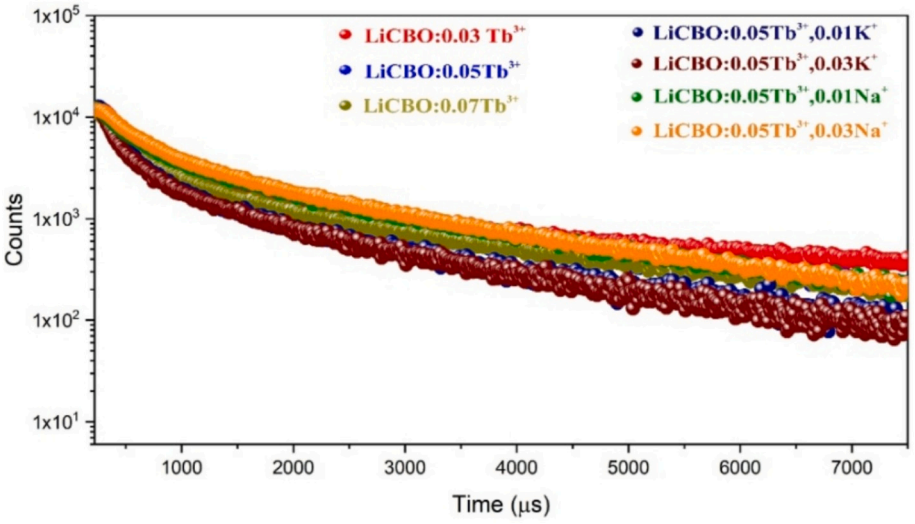

Fig. 11. Time-resolved luminescence decay curves of LiCBO:Tb^{3+} and alkali-ion (K^+, Na^+) co-doped LiCBO:Tb^{3+} phosphors recorded at room temperature.

Table 6
Decay lifetimes, relative contributions, average lifetime (τ_{avg}), and χ^2 values obtained from multi-exponential fitting of the luminescence decay curves of LiCBO:Tb^{3+} and alkali-ion co-doped samples.

		Time(μs)	Rel.%	τ_{avg}(μs)	χ^2
LiCBO:0.03Tb^{3+}	τ_1	19.84	20.18	1761.425	1.618
	τ_2	759.16	30.61		
	τ_3	1858.03	49.21		
LiCBO:0.05Tb^{3+}	τ_1	20.22	24.09	1701.257	1.485
	τ_2	775.39	29.15		
	τ_3	1783.95	46.76		
LiCBO: 0.07 Tb^{3+}	τ_1	18.99	22.69	1804.008	1.394
	τ_2	801.74	28.43		
	τ_3	2057.77	48.88		
LiCBO:0.05Tb^{3+},0.01 K^+	τ_1	25.49	32.33	1570.533	1.119
	τ_2	1620.84	67.67		
LiCBO:0.05Tb^{3+},0.03 K^+	τ_1	28.33	26.16	1598.171	1.405
	τ_2	705.97	36.62		
	τ_3	1859.61	37.22		
LiCBO:0.05Tb^{3+},0.01Na^+	τ_1	23.03	31.59	1611.450	1.666
	τ_2	1612.58	68.41		
LiCBO:0.05Tb^{3+},0.03Na^+	τ_1	21.11	21.41	1661.594	1.295
	τ_2	967.09	32.56		
	τ_3	1875.23	46.03		

corresponding relative amplitudes. The extracted decay parameters, including individual lifetimes, relative contributions, average lifetime (τ_{avg}), and goodness-of-fit (χ^2), are summarized in Table 6.

For the singly doped LiCBO:Tb^{3+}, a three-component decay is observed. The short lifetime component ($\tau_1 \approx$ 19–20 μs) is commonly associated with non-radiative recombination via surface defects or shallow traps, whereas the intermediate and long components (τ_2 and τ_3) originate from intrinsic Tb^{3+} $5D_4 \rightarrow 7F_j$ radiative transitions. With increasing Tb^{3+} concentration from 0.03 to 0.07, a slight increase in τ_{avg} is found, indicating enhanced energy migration among Tb^{3+} ions and improved radiative efficiency up to an optimal doping level.

In alkali-ion co-doped samples, a marked modification of the decay dynamics is observed. The LiCBO:0.05Tb^{3+},0.01 K^+ and LiCBO:0.05Tb^{3+},0.01Na^+ phosphors show predominantly bi-exponential decay with reduced τ_{avg} and improved χ^2 values, implying more efficient radiative recombination and suppressed defect-related quenching. This can be attributed to K^+/Na^+ acting as charge compensators that reduce non-radiative centers and refine the local crystal field around Tb^{3+} [23,42].

However, at higher alkali-ion contents (0.03 K^+ and 0.03Na^+), the decay curves again become three-exponential, accompanied by a slight increase in τ_{avg}. This suggests that excess alkali incorporation induces additional lattice distortions or defect sites, partially offsetting the beneficial charge-compensation effect [26].

Overall, the time-resolved measurements demonstrate that both Tb^{3+} concentration and alkali co-doping are decisive parameters for tailoring the luminescence decay dynamics of LiCBO-based phosphors. In particular, low-level K^+/Na^+ co-doping optimizes the decay behavior by efficiently suppressing non-radiative recombination pathways, which is fully consistent with the enhanced steady-state photoluminescence performance.

4.6. Judd–Ofelt analysis of $LiCa_4O(BO_3)_3$:Tb^{3+} phosphors

To understand the radiative properties and site symmetry of Tb^{3+} ions in LiCBO phosphors, a detailed Judd–Ofelt (J–O) analysis was performed for the undoped and co-doped samples. Emission spectra were recorded under 378 nm excitation, and the integrated intensities of the $^5D_4 \rightarrow 7F_J$ (J = 6–0) transitions were obtained by Gaussian fitting. The magnetic dipole transition $^5D_4 \rightarrow {}^7F_5$ at 542 nm was used as the internal reference, since its intensity is largely unaffected by the local crystal field.

The experimental oscillator strengths (f_{exp}) were calculated using the relation:

$$f_{exp} = \frac{mc^3}{8\pi^2 n^2 \nu^2 N_A} \bullet \frac{I_J}{\sum I_J}$$

where m is the electron mass, c is the speed of light, n is the refractive index (estimated as 1.6 in the UV–visible region based on typical borate hosts), ν is the transition frequency, N_A is Avogadro's number, and (I_J) is the integrated intensity of the $^5D_4 \rightarrow 7F_J$ transition.

The electric dipole transition probability (A_J) for $^5D_4 \rightarrow 7F_J$ transitions (J ≠ 5) was calculated using:

$$A_J = \frac{64\pi^4 e^2 \nu^3}{3h(2J+1)} n\left(\frac{n^2+2}{9}\right)^2 \sum_{\lambda=2,4,6} \Omega_\lambda \langle 5D_4 \| U^{(\lambda)} \| 7F_J \rangle^2$$ The magnetic dipole transition probability for $5D_4 \rightarrow 7F_5$ was calculated as:

$$A_{md} = \frac{64\pi^4 \nu^3 n^3 S_{md}}{3h(2J'+1)}$$

where (S_{md}) is the magnetic dipole line strength, and $\langle 5D_4 \| U^{(\lambda)} \| 7F_J \rangle^2$ are the squared reduced matrix elements, taken from Carnall et al. [90].

The radiative lifetime (τ_{rad}) and branching ratio (β_J) were evaluated using:

$$\tau_{rad} = \frac{1}{\sum A_J}; \qquad \beta_J = \frac{A_J}{\sum A_J}$$

The Judd–Ofelt parameters Ω_2, Ω_4, and Ω_6 were obtained by least-squares fitting of the experimental oscillator strengths to the theoretical values derived from the above expressions. The fitted values for each composition, along with the derived radiative properties, are summarized in Table 7.

These results confirm that co-doping subtly modifies the optical environment of Tb^{3+} in LiCBO, thereby tuning the emission characteristics while preserving high radiative efficiency. The increase in (Ω_2) for co-doped samples is especially indicative of enhanced asymmetry in the ligand field due to the presence of monovalent alkali ions. Moreover, the increase in the Ω_2 parameter, together with the slight enhancement of the Ω_2/Ω_4 ratio in the alkali co-doped samples, is consistent with the

Table 7
Judd–Ofelt intensity parameters Ω_2, Ω_4, and Ω_6, radiative transition probability ($A_{^5D_4 \rightarrow {}^7F_5}$), calculated radiative lifetime τ_{rad}, and internal quantum efficiency (η), asymmetry ratio Ω_2/Ω_4 and experimental oscillator strength f_{exp} for LiCBO:Tb^{3+} samples.

Sample composition	Ω_2 ($\times 10^{-20}$ cm^2)	Ω_4 ($\times 10^{-20}$ cm^2)	Ω_6 ($\times 10^{-20}$ cm^2)	Ω_2/Ω_4	($A_{^5D_4 \rightarrow {}^7F_5}$) ($s^{-1}$)	τ_{rad}(μs)	η	f_{exp} (arb. Units)
0.05Tb^{3+}	0.45	1.12	0.73	0.40	91.5	1980	0.85	3.21
0.05Tb^{3+}, 0.01 K^+	0.49	1.17	0.76	0.42	89.6	1925	0.82	3.25
0.05Tb^{3+},0.01Na^+	0.47	1.15	0.75	0.41	90.8	1954	0.83	3.28

locally enhanced asymmetry of the Tb^{3+} ligand field inferred from FTIR/Raman band shifts and alkali-ion-assisted charge-compensated lattice modification.

The Judd–Ofelt intensity parameters and derived radiative properties obtained for LiCBO:Tb^{3+} phosphors were compared with those reported for structurally distinct Tb^{3+}-doped hosts such as $GdAlO_3$, $Y_4Al_2O_9$, and $BaLaGaO_4$. Notably, the Ω_2 values in the present work (0.45–0.49 × 10^{-20} cm^2) fall within the typical range observed for borate and aluminate hosts, indicating a moderately asymmetric ligand environment. This level of asymmetry is sufficient to enable strong

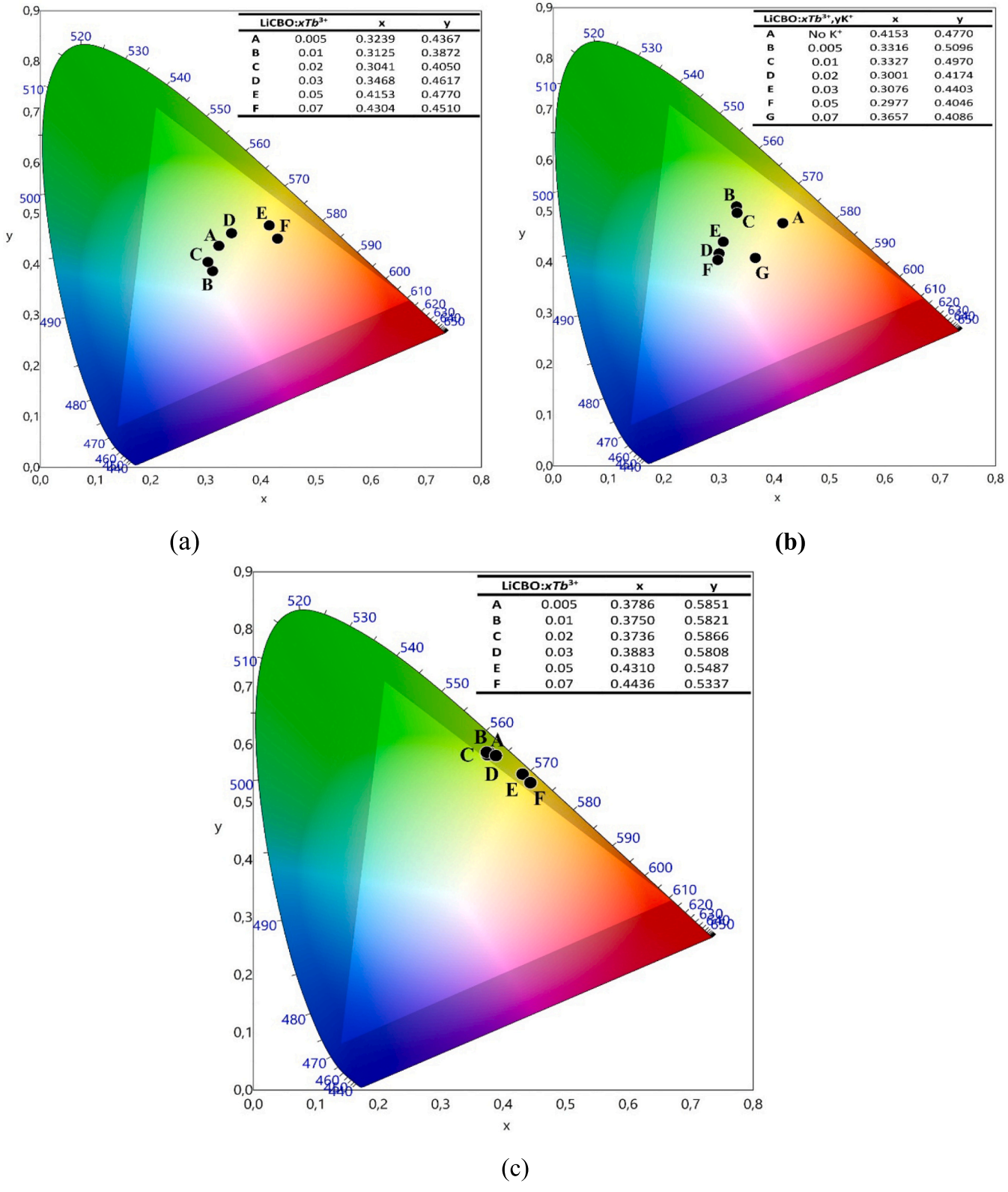

Fig. 12. CIE 1931 chromaticity coordinates of LiCBO:Tb^{3+} phosphors: (a) Tb^{3+}-only samples without alkali codoping, and Tb^{3+} samples codoped with (b) K^+ and (c) Na^+, illustrating the effect of alkali-ion incorporation on emission color and chromatic stability.

electric dipole transitions while preserving lattice stability. The slight increase in Ω_2 upon alkali co-doping further confirms the local distortion induced by monovalent ions. The calculated radiative lifetimes (1925–1980 μs) and internal quantum efficiencies (η = 82–85%) are slightly higher than or comparable to those reported for similar compositions. This indicates minimal non-radiative losses and reflects a well-optimized crystal field environment around Tb^{3+} ions in the LiCBO host. As a result, efficient $^5D_4 \rightarrow {}^7F_j$ radiative transitions are facilitated, demonstrating the favorable luminescent performance of this matrix [68].

4.7. Chromaticity coordinates and correlated color temperature analysis

Fig. 12a–c shows the CIE 1931 chromaticity coordinates of LiCBO:Tb^{3+} phosphors as a function of composition: (a) Tb^{3+}-only samples without alkali co-doping, and Tb^{3+} samples co-doped with (b) K^+ and (c) Na^+. In the Tb^{3+}-only series (Fig. 12a), variation of Tb^{3+} concentration results in a systematic shift of the emission coordinates within the green region toward yellowish-green, reflecting changes in the relative intensities of the characteristic Tb^{3+} emission transitions. For the K^+-co-doped samples (Fig. 12b), the chromaticity coordinates exhibit a wider distribution, especially at lower K^+ contents, indicating more effective color tuning through alkali incorporation. At higher K^+ concentrations, the coordinates move closer to the central region of the diagram, suggesting a partial reduction in green color saturation due to modifications in the local crystal field around Tb^{3+} ions. In contrast, the Na^+-co-doped samples (Fig. 12c) show a more compact clustering of chromaticity points, implying improved color stability against compositional changes. The emission remains confined to the green–yellow-green region, with smaller coordinate shifts compared to the K^+-co-doped series.

The correlated color temperature (CCT) values were estimated from the CIE chromaticity coordinates by locating the nearest point on the Planckian locus. For the Tb^{3+}-only series, the CCT values span a wide range, decreasing from approximately 6400 K at lower Tb^{3+} contents to about 3450 K at higher concentrations, with an average CCT lying in the neutral-white region. This trend reflects the gradual chromaticity shift toward longer wavelengths with increasing Tb^{3+} content. In the K^+-co-doped samples, a broader CCT distribution is observed, ranging from around 4500 K to nearly 6700 K, indicating enhanced tunability but reduced chromatic stability. This wide variation is consistent with the larger dispersion of chromaticity coordinates seen in Fig. 12b. By contrast, the Na^+-co-doped series exhibits comparatively stable CCT values, mostly confined between 5300 K and 5700 K, with an average close to 5500 K, corresponding to the cool-white region. The narrower CCT spread supports the observed clustering of chromaticity coordinates and confirms the superior color stability achieved through Na^+ co-doping.

From a chromaticity-engineering perspective, the CIE 1931 coordinates and corresponding CCT values obtained for $LiCa_4O(BO_3)_3$:Tb^{3+} establish a quantitative connection between the spectroscopic emission characteristics and practical solid-state lighting requirements. In all compositions, the emission is confined to the green–yellowish-green region of the CIE diagram, overlapping with the chromaticity domain commonly targeted by Tb^{3+}-activated green phosphors in near-UV pumped LED systems.

For the Tb^{3+}-only series, the calculated CCT values span ≈6400 K to ≈3450 K with increasing Tb^{3+} concentration, indicating that compositional tuning enables modulation of the effective green-channel contribution when integrated into multi-phosphor white-LED architectures. In contrast, Na^+ co-doping yields a narrower CCT distribution (≈5300–5700 K), centred near ≈5500 K, which aligns with the cool-white region typically employed in commercial NUV-pumped WLED modules.

Importantly, the temperature-dependent PL results demonstrate negligible spectral shift between 300 and 550 K, implying preservation of the chromaticity coordinates under realistic LED junction temperatures. This thermal chromatic stability is essential for maintaining color consistency in high-power devices.

Taken together, these results indicate that Tb^{3+} activation in $LiCa_4O(BO_3)_3$ provides controlled green emission within practical SSL chromaticity windows while maintaining thermally stable chromatic coordinates under device-relevant operating conditions.

Overall, these results indicate that K^+ co-doping enables broader color tunability at the expense of chromatic stability, whereas Na^+ co-doping favors color stability and a relatively constant cool-white emission window.

5. Conclusions

This work demonstrates that charge-compensated Tb^{3+} activation in LiCBO can be effectively engineered to deliver strong green emission, high-temperature stability, and competitive thermometric performance. Alkali-assisted charge compensation systematically improves crystallinity, relieves microstrain, and homogenizes the defect landscape, while preserving the intrinsic borate framework and Tb^{3+} site preference, thereby providing a structurally robust platform for optical optimization.

On the photophysical side, the LiCBO host sustains a relatively high optimum Tb^{3+} concentration with multipolar-governed concentration quenching and non-single-exponential decay, reflecting efficient activator–activator coupling in a rigid, low-phonon matrix Li^+/Na^+ co-doping enhances the usable green output by suppressing defect-assisted channels and modestly increasing local asymmetry, as evidenced by the evolution of lifetime components and Judd–Ofelt parameters, without compromising color purity or chromatic stability.

Thermally, LiCBO:Tb^{3+} retains a substantial fraction of its green emission up to LED-relevant junction temperatures and exhibits a single dominant thermal quenching channel with a moderate-to-high activation barrier. Moreover, the 680/542 nm fluorescence intensity ratio readout affords relative sensitivities up to ~1.3% K^{-1} near 500 K, demonstrating competitive performance among single-ion Tb^{3+}-based thermometric phosphors at elevated temperatures. Overall, these findings establish LiCBO:Tb^{3+} as a versatile borate platform and highlight alkali-ion charge compensation as an effective design strategy for thermally robust green phosphors and single-center luminescent thermometers.

CRediT authorship contribution statement

Abeer S. Altowyan: Writing – original draft, Methodology, Investigation, Funding acquisition, Formal analysis. **M.B. Coban:** Software, Methodology, Investigation, Funding acquisition. **U.H. Kaynar:** Methodology, Investigation, Formal analysis. **R. Tulek:** Methodology, Investigation. **A. Teke:** Methodology, Investigation. **Y. Ozcan:** Methodology, Investigation. **Jabir Hakami:** Methodology, Investigation, Conceptualization. **H. Aydin:** Software, Methodology, Investigation. **N. Can:** Writing – review & editing, Writing – original draft, Supervision.

Declaration of competing interest

The authors declare that they have no known competing financial interests or personal relationships that could have appeared to influence the work reported in this paper.

Acknowledgements

We would like to express our sincere gratitude to the Research Funds of Balikesir University (Grant No. BAP-2025/014) for the financial support. This study was also supported by the Princess Nourah bint Abdulrahman University Researchers Supporting Project number (PNURSP2026R16), Princess Nourah bint Abdulrahman University, Riyadh, Saudi Arabia.

Data availability

Data will be made available on request.

References

[1] I. Gupta, S. Singh, S. Bhagwan, D. Singh, Rare earth (RE) doped phosphors and their emerging applications: a review, Ceram. Int. 47 (2021) 19282–19303, https://doi.org/10.1016/j.ceramint.2021.03.308.

[2] Y.R. Parauha, N.T. Kalyani, S.J. Dhoble, Recent trends in rare earth doped luminescent materials: a review, J. Mol. Struct. 1347 (2025) 143190, https://doi.org/10.1016/j.molstruc.2025.143190.

[3] X. Huang, B. Li, H. Guo, Synthesis, photoluminescence, cathodoluminescence, and thermal properties of novel Tb^{3+}-doped BiOCl green-emitting phosphors, J. Alloys Compd. 695 (2017) 2773–2780, https://doi.org/10.1016/j.jallcom.2016.11.224.

[4] S. Yusan, M.B. Coban, U.H. Kaynar, I.G. Kaptanoglu, A.S. Altowyan, J. Hakami, H. Aydin, E.E. Karali, A. Canimoglu, N. Can, Structural and luminescence analysis of Li^{+}/Na^{+} co-doped $K_7CaGd_2(B_5O_{10})_3$:Tb^{3+} phosphors with enhanced green emission and thermal stability, Mater. Res. Bull. 198 (2026) 114011, https://doi.org/10.1016/j.materresbull.2026.114011.

[5] U. Fawad, H.J. Kim, I. Gul, M. Khan, S. Tahir, T. Jamal, W. Muhammad, Proton, UV, and X-ray induced luminescence in Tb^{3+} doped $LuGd_2Ga_2Al_3O_{12}$ phosphors, Crystals 10 (2020) 844, https://doi.org/10.3390/cryst10090844.

[6] G. Blasse, B.C. Grabmaier, Luminescent Materials, Springer Berlin Heidelberg, Berlin, Heidelberg, 1994, https://doi.org/10.1007/978-3-642-79017-1.

[7] S. Kaur, A.S. Rao, M. Jayasimhadri, V.V. Jaiswal, D. Haranath, Tb^{3+} ion induced colour tunability in calcium aluminozincate phosphor for lighting and display devices, J. Alloys Compd. 826 (2020) 154212, https://doi.org/10.1016/j.jallcom.2020.154212.

[8] J. Ueda, A. Meijerink, P. Dorenbos, A.J.J. Bos, S. Tanabe, Thermal ionization and thermally activated crossover quenching processes for 5d–4f luminescence in $Y_3Al_{5-x}Ga_xO_{12}$:Pr^{3+}, Phys. Rev. B 95 (2017) 014303 https://doi.org/10.1103/PhysRevB.95.014303.

[9] M.A. van de Haar, M. Tachikirt, A.C. Berends, M.R. Krames, A. Meijerink, F. T. Rabouw, Saturation mechanisms in common LED phosphors, ACS Photonics 8 (2021) 1784–1793, https://doi.org/10.1021/acsphotonics.1c00372.

[10] N. Jaidass, C. Krishna Moorthi, A. Mohan Babu, M. Reddi Babu, Luminescence properties of Dy^{3+} doped lithium zinc borosilicate glasses for photonic applications, Heliyon 4 (2018) e00555, https://doi.org/10.1016/j.heliyon.2018.e00555.

[11] Y. Gao, X. Zhu, H. Shi, P. Jiang, R. Cong, T. Yang, Eu^{3+} and Tb^{3+} doped $LiCaY_5(BO_3)_6$: efficient red and green phosphors under UV or NUV excitations, JOL 242 (2022) 118598, https://doi.org/10.1016/j.jlumin.2021.118598.

[12] Y. Li, Z. Dong, S. Xu, C. Wu, J. Chen, C. Zhang, H. Qi, X. Zhang, H. Liu, Y. Chi, X. Sun, C.K. Mahadevan, Photoluminescence and thermoluminescence performance in Tb^{3+}-activated aluminum borosilicate glass with high thermal stability for blue-green laser and TLD applications, Ceram. Int. 50 (2024) 38445–38455, https://doi.org/10.1016/j.ceramint.2024.07.209.

[13] A. Tiwari, S.J. Dhoble, Borate-based luminescent materials: a comprehensive review of structural influences on thermal stability and luminescence characteristics, JOL 287 (2025) 121490, https://doi.org/10.1016/j.jlumin.2025.121490.

[14] G. Souadi, A.Y. Madkhli, U.H. Kaynar, C. Gok, H. Aydin, M.B. Coban, S.C. Kaynar, M. Ayvacikli, N. Can, Photoluminescence properties and structural analysis of Tb^{3+}-doped $K_3Gd(BO_2)_6$: a first study on negative thermal quenching, J. Alloys Compd. 1010 (2025) 178147, https://doi.org/10.1016/j.jallcom.2024.178147.

[15] S.B. Töreli, V.E. Kafadar, F.M. Emen, E. Öztürk, R. Altınkaya, Synthesis and photoluminescence properties of Eu^{3+}-activated $Ba_2Cd(BO_3)_2$ red-emitting phosphors for near-ultraviolet excited white light-emitting diodes, Luminescence 40 (2025), https://doi.org/10.1002/bio.70135.

[16] T. Pier, T. Jüstel, Activator – host structure relations of applied optical materials: a review, Z. Krist. - Cryst. Mater. 240 (2025) 197–247, https://doi.org/10.1515/zkri-2025-0019.

[17] İ. Pekgözlü, E. Erdoğmuş, A.S. Başak, Synthesis and photoluminescence properties of Pb^{2+} doped $Li_4CaB_2O_6$, Optik 126 (2015) 1221–1223, https://doi.org/10.1016/j.ijleo.2015.04.002.

[18] M. Sharma, H. Sharma, I. Charak, H.C. Swart, V. Kumar, Optimization and luminescence studies of Sm^{3+} doped $LiCaBO_3$ phosphors for high-performance white light-emitting diodes, Chem. Phys. Impact 9 (2024) 100696, https://doi.org/10.1016/j.chphi.2024.100696.

[19] M.B. Coban, J. Hakami, H. Aydin, U.H. Kaynar, E. Aymila Çin, T. Karaman, M. Sharahili, O. Madkhali, D. Somaily, R. Karmouch, N. Can, Structural and luminescence properties of alkali-co-doped $LiCaBO_3$:Dy^{3+} phosphors, Appl. Radiat. Isot. 227 (2026) 112288, https://doi.org/10.1016/j.apradiso.2025.112288.

[20] A.S. Altowyan, U.H. Kaynar, H. Aydin, J. Hakami, M.B. Coban, K. Cikrikci, M. Ayvacikli, N. Can, Synthesis, structural characterization, and photoluminescence properties of Dy^{3+}-doped CaB_4O_7 phosphors: influence of Li+ and K+ co-doping, Mater. Sci. Semicond. Process. 195 (2025) 109593, https://doi.org/10.1016/j.mssp.2025.109593.

[21] J. Hakami, M.B. Coban, H. Aydin, U.H. Kaynar, M. Sharahili, O. Madkhali, D. Somaily, N. Can, Structural modulation and Judd–Ofelt-guided luminescence enhancement in Eu^{3+}-doped $LiCa_4O(BO_3)_3$ via dual-alkali co-doping, JOL 289 (2026) 121670, https://doi.org/10.1016/j.jlumin.2025.121670.

[22] A.K. Singh, S.K. Singh, S.B. Rai, Role of Li^{+} ion in the luminescence enhancement of lanthanide ions: favorable modifications in host matrices, RSC Adv. 4 (2014) 27039–27061, https://doi.org/10.1039/C4RA01055H.

[23] V.R. Mala, A. Princy, K.J. Albert, S.M. Moses Kennedy, Enhancement of green light emission from the $LiSrVO_4$:Tb^{3+} doped vanadate phosphor by charge compensation via co-doping of the alkali metal ions (Li^{+}/Na^{+}/K^{+}), JOL 263 (2023) 119948, https://doi.org/10.1016/j.jlumin.2023.119948.

[24] H. Orucu, A.S. Altowyan, U.H. Kaynar, H. Aydin, M.B. Coban, J. Hakami, N. Can, Synthesis, structural characterization, and photoluminescence behavior of $NaCa_4(BO_3)_3$:Tb^{3+} phosphors co-doped with K^{+}: insights into radiation-induced defect formation and charge compensation via DFT calculations, Appl. Radiat. Isot. 225 (2025) 112038, https://doi.org/10.1016/j.apradiso.2025.112038.

[25] G.W. Jung, K. Park, Effect of monovalent charge compensators on the photoluminescence properties of $Ca_3(PO_4)_2$:Tb^{3+}, a^{+} (a = Li, Na, K) phosphors, J. Mater. Sci. Technol. 82 (2021) 187–196, https://doi.org/10.1016/j.jmst.2020.11.065.

[26] P.N. Parale, A.R. Kadam, S.J. Dhoble, K.V. Dabre, Tailored efficient energy transfer Tb^{3+}, Eu^{3+} activated/co-activated $LiAl(PO_3)_4$ phosphor by substitution of alkali metals: the effect of charge compensation, RSC Adv. 13 (2023) 26179–26188, https://doi.org/10.1039/D3RA03115B.

[27] Q. Zhang, R. Lou, Z. Liu, W. Feng, Blue-green luminescence properties and charge compensation of $Ca_9MgLi(PO_4)_7$ doped with Tb^{3+} and alkali metal ions, Z. Naturforsch. A 78 (2023) 263–269, https://doi.org/10.1515/zna-2022-0208.

[28] M. Zheng, W. Zhang, Q. Ou, J. Tang, Investigation of preparation and photoluminescence properties of europium-doped calcium orthoborate ($ca_3B_2O_6$:Eu^{3+}) red phosphor and red LED, Ceram. Int. 50 (24) (2024) 53618–53627, https://doi.org/10.1016/j.ceramint.2024.10.211.

[29] M. Behera, R. Panda, R.A. Kumar, N.K. Mishra, K. Kumar, T. Del Monte, Microwave-assisted combustion synthesis and characterization studies of novel dysprosium-doped yttrium calcium borate (Dy^{3+}:$Y_2CaB_{10}O_{19}$) phosphor materials for efficient white light applications, Ceram. Int. 50 (11) (2024) 18146–18156, https://doi.org/10.1016/j.ceramint.2024.02.298.

[30] Y. Wang, G. Li, M. Zeng, Y. Hu, H. Guo, Y. Li, Synthesis and photoluminescence properties of single-phase $Sr_3B_{14}O_{24}$:RE^{3+} (RE = Ce, Tb, Sm, Eu) phosphors and glass for WLEDs, UV and NIR shielding, Ceram. Int. 50 (4) (2024) 6278–6288, https://doi.org/10.1016/j.ceramint.2023.11.356.

[31] X.B. Li, W.B. Dai, K. Nie, S.P. Li, M. Xu, Investigation on optical properties of borate $Sr_3Y_2B_4O_{12}$:Ce/Tb/Sm and its application in WLEDs, JOL 263 (2023) 120038, https://doi.org/10.1016/j.jlumin.2023.120038.

[32] A.T. Hines, G. Morrison, B.J. Yarbrough, N.B. Shustova, L.G. Jacobsohn, zur Loye, H.-C., Luminescence of alkali rare earth borates $A_3Ln(BO_3)_2$ (A = Na, K; Ln = Eu, Tb), Solid State Sci. 138 (2023) 107130, https://doi.org/10.1016/j.solidstatesciences.2023.107130.

[33] A.S. Altowyan, M.B. Coban, U.H. Kaynar, J. Hakami, M. Ayvacikli, A. Hiziroglu, N. Can, Temperature-dependent photoluminescence of novel Eu^{3+}, Tb^{3+}, and Dy^{3+} doped $LaCa_4O(BO_3)_3$: insights at low and room temperatures, Appl. Radiat. Isot. 208 (2024) 111308, https://doi.org/10.1016/j.apradiso.2024.111308.

[34] J. Tang, J. Si, X. Fan, Y. Liu, G. Li, G. Cai, Tunable emission, energy transfer and thermal stability of Ce^{3+}, Tb^{3+} co-doped $Na_2BaCa(PO_4)_2$ phosphors, J. Rare Earths 40 (2022) 878–887, https://doi.org/10.1016/j.jre.2021.05.016.

[35] A.A. Alsam, U.H. Kaynar, H. Aydin, M.B. Coban, A. Canimoglu, N. Can, Enhanced luminescence and quenching mechanisms in Na^{+} co-doped $K_7CaY_2(B_5O_{10})_3$:Tb^{3+} phosphors under UV radiation, Appl. Radiat. Isot. 217 (2025) 111635, https://doi.org/10.1016/j.apradiso.2024.111635.

[36] R.D. Shannon, C.T. Prewitt, Effective ionic radii in oxides and fluorides, Acta Crystallogr. Sect. B Struct. Crystallogr. Cryst. Chem. 25 (1969) 925–946, https://doi.org/10.1107/S0567740869003220.

[37] A.A.B. Baloch, S.M. Alqahtani, F. Mumtaz, A.H. Muqaibel, S.N. Rashkeev, F. H. Alharbi, Extending Shannon's ionic radii database using machine learning, Phys. Rev. Mater. 5 (2021) 043804, https://doi.org/10.1103/PhysRevMaterials.5.043804.

[38] H.E. Mgbemere, M. Hinterstein, G.A. Schneider, Electrical and structural characterization of $(K_xNa_{1-x})NbO_3$ ceramics modified with Li and ta, J. Appl. Cryst. 44 (2011) 1080–1089, https://doi.org/10.1107/S0021889811027701.

[39] T. He, L. Chen, Y. Su, Y. Lu, L. Bao, G. Chen, Q. Zhang, S. Chen, F. Wu, The effects of alkali metal ions with different ionic radii substituting in Li sites on the electrochemical properties of Ni-rich cathode materials, J. Power Sources 441 (2019) 227195, https://doi.org/10.1016/j.jpowsour.2019.227195.

[40] R.L. Tranquilin, L.X. Lovisa, C.R.R. Almeida, C.A. Paskocimas, M.S. Li, M. C. Oliveira, L. Gracia, J. Andres, E. Longo, F.V. Motta, M.R.D. Bomio, Understanding the white-emitting $CaMoO_4$ co-doped Eu^{3+}, Tb^{3+}, and Tm^{3+} phosphor through experiment and computation, J. Phys. Chem. C 123 (2019) 18536–18550, https://doi.org/10.1021/acs.jpcc.9b04123.

[41] P. Kumar, D. Singh, S. Kadyan, H. Kumar, R. Kumar, Cool green-emissive $Y_2Si_2O_7$: Tb^{3+} nanophosphor: auto-combustion synthesis and structural and photoluminescence characteristics with good thermal stability for lighting applications, RSC Adv. 14 (2024) 16560–16573, https://doi.org/10.1039/D4RA02571G.

[42] S.C. Kaynar, A.S. Altowyan, H. Aydin, U.H. Kaynar, M.B. Coban, J. Hakami, N. Can, Judd–Ofelt analysis and photoluminescence behavior of Tb^{3+}-activated $K_7SrY_2(B_5O_{10})_3$ phosphors modified with alkali co-dopants for solid-state lighting applications, Spectrochim. Acta. Part A Mol. Biomol. Spectrosc. 341 (2025) 126435, https://doi.org/10.1016/j.saa.2025.126435.

[43] T. Zhang, Z. Guo, H. Yang, F. Zhao, Q. Mao, X. Li, M. Liu, J. Zhong, The defect regulation engineering based on alkaline metal for enhancing the long persistent

luminescence and thermal stability, Laser Photon. Rev. (2025), https://doi.org/10.1002/lpor.202502092.
[44] D. Nath, F. Singh, R. Das, X-ray diffraction analysis by Williamson-Hall, Halder-Wagner and size-strain plot methods of CdSe nanoparticles- a comparative study, Mater. Chem. Phys. 239 (2020) 122021, https://doi.org/10.1016/j.matchemphys.2019.122021.
[45] M. Kawsar, M.S. Hossain, N.M. Bahadur, S. Ahmed, Synthesis of nano-crystallite hydroxyapatites in different media and a comparative study for estimation of crystallite size using Scherrer method, Halder-Wagner method size-strain plot, and Williamson-Hall model, Heliyon 10 (2024) e25347, https://doi.org/10.1016/j.heliyon.2024.e25347.
[46] M. İlhan, L.F. Güleryüz, M.İ. Katı, Exploring the effect of boron on the grain morphology change and spectral properties of Eu^{3+} activated barium tantalate phosphor, RSC Adv. 14 (2024) 2687–2696, https://doi.org/10.1039/D3RA08197D.
[47] S.K. Sen, U.C. Barman, M.S. Manir, P. Mondal, S. Dutta, M. Paul, M.A. M. Chowdhury, M.A. Hakim, X-ray peak profile analysis of pure and Dy-doped α -MoO_3 nanobelts using Debye-Scherrer, Williamson-Hall and Halder-Wagner methods, Adv. Nat. Sci. Nanosci. Nanotechnol. 11 (2020) 025004, https://doi.org/10.1088/2043-6254/ab8732.
[48] S.A. Khan, T. Ahmed, H.W. Park, M. Habib, T.K. Song, C. Wang, S.U. Mun, Y. Kim, M.-H. Kim, S. Lee, Effects of B- and A/B-sites Codoping on lattice distortion and defect concentration for high electromechanical response of lead-free piezoelectrics, Acta Mater. 278 (2024) 120262, https://doi.org/10.1016/j.actamat.2024.120262.
[49] S.A. Disha, M. Sahadat Hossain, M.L. Habib, S. Ahmed, Calculation of crystallite sizes of pure and metals doped hydroxyapatite engaging Scherrer method, Halder-Wagner method, Williamson-Hall model, and size-strain plot, Results Mater. 21 (2024) 100496, https://doi.org/10.1016/j.rinma.2023.100496.
[50] S. Yousefi, B. Ghasemi, M.P. Nikolova, Morpho/opto-structural characterizations and XRD-assisted estimation of crystallite size and strain in MgO nanoparticles by applying Williamson–Hall and size–strain techniques, J. Clust. Sci. 33 (2022) 2197–2207, https://doi.org/10.1007/s10876-021-02144-y.
[51] M. Basak, M.L. Rahman, M.F. Ahmed, B. Biswas, N. Sharmin, The use of X-ray diffraction peak profile analysis to determine the structural parameters of cobalt ferrite nanoparticles using Debye-Scherrer, Williamson-Hall, Halder-Wagner and size-strain plot: different precipitating agent approach, J. Alloys Compd. 895 (2022) 162694, https://doi.org/10.1016/j.jallcom.2021.162694.
[52] A.A. Al-Tabbakh, N. Karatepe, A.B. Al-Zubaidi, A. Benchaabane, N.B. Mahmood, Crystallite size and lattice strain of lithiated spinel material for rechargeable battery by X-ray diffraction peak-broadening analysis, Int. J. Energy Res. 43 (2019) 1903–1911, https://doi.org/10.1002/er.4390.
[53] M.M. Hivrekar, D.B. Sable, M.B. Solunke, K.M. Jadhav, Network structure analysis of modifier CdO doped sodium borate glass using FTIR and Raman spectroscopy, J. Non Cryst. Solids 474 (2017) 58–65, https://doi.org/10.1016/j.jnoncrysol.2017.08.028.
[54] E. Abou Hussein, Gamma rays interactions on optical, FTIR and ESR spectra of alkaline earth binary borate glasses, Arab J. Nucl. Sci. Appl. 53 (2020) 1–18, https://doi.org/10.21608/ajnsa.2020.17460.1278.
[55] Y.H. Elbashar, S.G. ElGabaly, D.A. Rayan, FTIR and NIR spectroscopic analyses of Co_3O_4-doped sodium zinc borate glass matrix, J. Opt. 50 (2021) 559–568, https://doi.org/10.1007/s12596-021-00724-9.
[56] R. Kaindl, G. Sohr, H. Huppertz, Experimental determinations and quantum-chemical calculations of the vibrational spectra of β-ZnB_4O_7 and β-CaB_4O_7, Spectrochim. Acta Part A Mol. Biomol. Spectrosc. 116 (2013) 408–417, https://doi.org/10.1016/j.saa.2013.07.072.
[57] A.M. Saleh, A.M. Abdelghany, W.M. Awad, Structural investigation and effect of gamma-ray irradiation on barium borate glasses containing vanadium oxide, Radiat. Phys. Chem. 217 (2024) 111513, https://doi.org/10.1016/j.radphyschem.2024.111513.
[58] M. Farouk, A. Samir, A. Ibrahim, M.A. Farag, A. Solieman, Raman, FTIR studies and optical absorption of zinc borate glasses containing WO3, Appl. Phys. A Mater. Sci. Process. 126 (2020) 696, https://doi.org/10.1007/s00339-020-03890-y.
[59] D. Möncke, E.I. Kamitsos, D. Palles, R. Limbach, A. Winterstein-Beckmann, T. Honma, Z. Yao, T. Rouxel, L. Wondraczek, Transition and post-transition metal ions in borate glasses: borate ligand speciation, cluster formation, and their effect on glass transition and mechanical properties, J. Chem. Phys. 145 (2016) 124501, https://doi.org/10.1063/1.4962323.
[60] A.M. Abdel-karim, A.M. Fayad, I.M. El-kashef, H.A. Saleh, Influence of vanadium oxide on the optical and electrical properties of Li (oxide or fluoride) borate glasses, J. Electron. Mater. 52 (2023) 2409–2420, https://doi.org/10.1007/s11664-022-10187-8.
[61] R.G. Nair, S. Nigam, V. Sudarsan, R.K. Vatsa, V.K. Jain, YBO_3 versus Y_3BO_6 host on Tb^{3+} luminescence, JOL 195 (2018) 271–277, https://doi.org/10.1016/j.jlumin.2017.11.038.
[62] S. Kaur, N. Deopa, A. Prasad, R. Bajaj, A.S. Rao, Intense green emission from Tb^{3+} ions doped zinc lead alumino borate glasses for laser and w-LEDs applications, Opt. Mater. 84 (2018) 318–323, https://doi.org/10.1016/j.optmat.2018.07.020.
[63] N. Huang, G. Lu, B. Bai, Z. Chen, M. Zhang, Y. Li, C. Cao, A. Xie, Preparation and photoluminescent properties of Tb^{3+}-doped $Lu_2W_3O_{12}$ and $Lu_2Mo_3O_{12}$ green phosphors, Chemosensors 10 (2022) 533, https://doi.org/10.3390/chemosensors10120533.
[64] J. Zhu, J. Xiang, Y. Mao, Near-UV-excited photoluminescence of terbium (III)-activated lithium sodium borophosphate phosphor, Optik 240 (2021) 166920, https://doi.org/10.1016/j.ijleo.2021.166920.
[65] N. Huang, G. Lu, B. Bai, H. Zhao, W. Yao, C. Cao, Y. Li, A. Xie, Preparation, crystal structure, and photoluminescence properties of Tb^{3+} activated $Lu_2(MoO_4)_3$ green-emitting phosphors, J. Lumin. 269 (2024) 120475, https://doi.org/10.1016/j.jlumin.2024.120475.
[66] D. Vijayasri, K.S. Rudramamba, T. Srikanth, N.M. Reddy, M. Nakka, S. Pratyusha, M.R. Reddy, Spectroscopic features of Tb^{3+} doped strontium zinc borate glasses for green laser applications, J. Mol. Struct. 1274 (f) 134514. doi:https://doi.org/10.1016/j.molstruc.2022.134514.
[67] O. Madkhali, Ü.H. Kaynar, Y. Alajlani, M.B. Coban, J.G. Guinea, M. Ayvacikli, J. F. Pierson, N. Can, Structural and temperature dependence luminescence characteristics of RE (RE=Eu^{3+}, Dy^{3+}, Sm^{3+} and Tb^{3+}) in the new gadolinium aluminate borate phosphor, Ceram. Int. 49 (2023) 19982–19995, https://doi.org/10.1016/j.ceramint.2023.03.120.
[68] P.K. Jisha, S.C. Prashantha, H. Nagabhushana, Luminescent properties of Tb doped gadolinium aluminate nanophosphors for display and forensic applications, J. Sci. Adv. Mater. Devices 2 (2017) 437–444, https://doi.org/10.1016/j.jsamd.2017.10.001.
[69] D.L. Dexter, J.H. Schulman, Theory of concentration quenching in inorganic phosphors, J. Chem. Phys. 22 (1954) 1063–1070, https://doi.org/10.1063/1.1740265.
[70] C.R. Kesavulu, A.C. Almeida Silva, M.R. Dousti, N.O. Dantas, A.S.S. de Camargo, T. Catunda, Concentration effect on the spectroscopic behavior of Tb^{3+} ions in zinc phosphate glasses, JOL 165 (2015) 77–84, https://doi.org/10.1016/j.jlumin.2015.04.012.
[71] U.H. Kaynar, H. Aydin, J. Hakami, A.S. Altowyan, M.B. Coban, M. Ayvacikli, A. Canimoglu, N. Can, Novel Tb^{3+}-doped $LaAl_2B_4O_{10}$ phosphors: structural analysis, luminescent properties, and energy transfer mechanism, Appl. Radiat. Isot. 210 (2024) 111380, https://doi.org/10.1016/j.apradiso.2024.111380.
[72] P. Halappa, A. Mathur, M.-H. Delville, C. Shivakumara, Alkali metal ion co-doped Eu^{3+} activated $GdPO_4$ phosphors: structure and photoluminescence properties, J. Alloys Compd. 740 (2018) 1086–1098, https://doi.org/10.1016/j.jallcom.2018.01.087.
[73] Z. Guo, H. Jiang, H. Li, H. Zhang, C. Liu, R. Zhao, Z. Yang, H. Tang, J. Li, J. Zhang, J. Zhu, Manipulating alkali charge compensation to improve red fluorescence and thermostability in $Ba_5P_6O_{20}$:Eu^{3+} phosphor, Appl. Mater. Today 37 (2024) 102095, https://doi.org/10.1016/j.apmt.2024.102095.
[74] B. Wang, Q. Ren, O. Hai, X. Wu, Luminescence properties and energy transfer in Tb^{3+} and Eu^{3+} co-doped $Ba_2P_2O_7$ phosphors, RSC Adv. 7 (2017) 15222–15227, https://doi.org/10.1039/C6RA28122B.
[75] V.G. Nosov, A.A. Betina, T.S. Bulatova, P.B. Guseva, I.E. Kolesnikov, S.N. Orlov, M. S. Panov, M.N. Ryazantsev, N.A. Bogachev, M.Y. Skripkin, A.S. Mereshchenko, Effect of Gd^{3+}, La^{3+}, Lu^{3+} co-doping on the morphology and luminescent properties of $NaYF_4$:Sm3+ phosphors, Materials (Basel) 16 (2023) 2157, https://doi.org/10.3390/ma16062157.
[76] C. Zhao, X. Kong, X. Liu, L. Tu, F. Wu, Y. Zhang, K. Liu, Q. Zeng, H. Zhang, Li^+ ion doping: an approach for improving the crystallinity and upconversion emissions of $NaYF_4$:Yb^{3+}, Tm^{3+} nanoparticles, Nanoscale 5 (2013) 8084, https://doi.org/10.1039/c3nr01916k.
[77] Q. Ren, Y. Zhao, X. Wu, O. Hai, Tb^{3+}/Eu^{3+}/Tm^{3+} co-doped single-phase phosphors emitting close to standard white light, Opt. Laser Technol. 136 (2021) 106774, https://doi.org/10.1016/j.optlastec.2020.106774.
[78] G. Souadi, O. Hakami, U.H. Kaynar, M.B. Coban, H. Aydin, O. Madkhali, T. Zelai, M. Ayvacikli, N. Can, High temperature photoluminescence dependence and energy migration of Tb^{3+}-incorporated $K_3Y(BO_2)_6$ phosphors, Appl. Radiat. Isot. 214 (2024) 111529, https://doi.org/10.1016/j.apradiso.2024.111529.
[79] Q. Li, C. Chen, Y. Qiao, B. Yu, B. Shen, Y. Zhang, High thermal stability of green-emitting phosphor $NaBaB_9O_{15}$: Tb^{3+} via energy compensation, J. Alloys Compd. 897 (2022) 163131, https://doi.org/10.1016/j.jallcom.2021.163131.
[80] Z. Lin, R. Huang, J. Song, Y. Zhang, Z. Lin, H. Li, H. Wu, D. Hou, Y. Guo, J. Wang, P.K. Chu, Enhancing negative thermal quenching in green-emitting perovskite microspheres via shallow trap state modulation, Sci. China-Mater. 68 (2025) 149–155, https://doi.org/10.1007/s40843-024-3134-1.
[81] C. Wang, Y. Cai, H. Zhang, Z. Liu, H. Lv, X. Zhu, Y. Liu, C. Wang, J. Qiu, X. Yu, X. Xu, Variation from zero to negative thermal quenching of phosphor with assistance of defect states, Inorg. Chem. 60 (2021) 19365–19372, https://doi.org/10.1021/acs.inorgchem.1c03188.
[82] H. Zhang, G. Fan, F. Ruan, Charge compensating effect of alkali metal ions R+ (R = Li, Na, K) on the luminescence enhancement of $CaAl_{11.9}P_{0.1}O_{19.1}$:$Mn^{4+}$ red-emitting phosphor, Inorg. Chem. Commun. 132 (2021) 108860, https://doi.org/10.1016/j.inoche.2021.108860.
[83] X. Yu, Z. Liu, W. Zhang, X. Xu, H. Du, Effect of A_+ (A = Li, Na and K) co-doping on enhancing the luminescence of $Ca_5(PO_4)_2SiO_4$:Eu^{3+} red-emitting phosphors as charge compensator, Ceram. Int. 47 (2021) 3540–3547, https://doi.org/10.1016/j.ceramint.2020.09.198.
[84] K.J. Albert, S.M.M. Kennedy, Unveiling the photoluminescence properties and thermal stability of blue-greenish to green light emitting Tb^{3+}-doped $NaBaBi_2(PO_4)_3$ phosphors, J. Fluoresc. 35 (2025) 11341–11354, https://doi.org/10.1007/s10895-025-04378-9.
[85] Y. Xiang, L. Yang, C. Liao, X. Xiang, X. Tang, H. Tang, J. Zhu, Thermometric properties of $Na_2Y_2TeB_2O_{10}$:Tb^{3+} green phosphor based on fluorescence/excitation intensity ratio, J. Adv. Ceram. 12 (2023) 848–860, https://doi.org/10.26599/JAC.2023.9220725.
[86] R. Lisiecki, J. Pisarska, W. Pisarski, W. Ryba-Romanowski, Study on temperature-sensitive factors relevant to thermographic features of Tb^{3+}-doped phosphate glasses, Mater. Res. Bull. 179 (2024) 112951, https://doi.org/10.1016/j.materresbull.2024.112951.

[87] J. Zhang, J. Chen, Y. Zhang, S. An, Yb^{3+}/Tm^{3+} and Yb^{3+}/Ho^{3+} doped $NaY_9(SiO_4)_6O_2$ phosphors: upconversion luminescence processes, temperature-dependent emission spectra and optical temperature-sensing properties, J. Alloys Compd. 860 (2021) 158473, https://doi.org/10.1016/j.jallcom.2020.158473.

[88] A. Xiakeer, L. Wang, M. Maimaiti, X. Feng, M. Jiang, Luminescence and temperature-sensing properties of Li^+, Na^+, or K^+, Tm^{3+}, and Yb^{3+} co-doped Bi_2WO_6 phosphors, Rev. Adv. Mater. Sci. 62 (2023), https://doi.org/10.1515/rams-2023-0104.

[89] Z. Wan, D. Xu, W. She, F. Xie, Y. Feng, J. Yang, G. Liu, X. Tong, Doping level dependence of the structure and luminescence properties of $LaBO_3:Tb^{3+}$ phosphors, Ceram. Int. 50 (2024) 9499–9509, https://doi.org/10.1016/j.ceramint.2023.12.268.

[90] W.T. Carnall, P.R. Fields, K. Rajnak, Electronic energy levels in the trivalent lanthanide aquo ions. I. Pr^{3+}, Nd^{3+}, Pm^{3+}, Sm^{3+}, Dy^{3+}, Ho^{3+}, Er^{3+}, and Tm^{3+}, J. Chem. Phys. 49 (1968) 4424–4442, https://doi.org/10.1063/1.1669893.